

CERN-EP-2023-257
2023/12/27

CMS-SMP-21-008

Measurement of multidifferential cross sections for dijet production in proton-proton collisions at $\sqrt{s} = 13$ TeV

The CMS Collaboration*

Abstract

A measurement of the dijet production cross section is reported based on proton-proton collision data collected in 2016 at $\sqrt{s} = 13$ TeV by the CMS experiment at the CERN LHC, corresponding to an integrated luminosity of up to 36.3 fb^{-1} . Jets are reconstructed with the anti- k_T algorithm for distance parameters of $R = 0.4$ and 0.8 . Cross sections are measured double-differentially (2D) as a function of the largest absolute rapidity $|y|_{\text{max}}$ of the two jets with the highest transverse momenta p_T and their invariant mass $m_{1,2}$, and triple-differentially (3D) as a function of the rapidity separation y^* , the total boost y_b , and either $m_{1,2}$ or the average p_T of the two jets. The cross sections are unfolded to correct for detector effects and are compared with fixed-order calculations derived at next-to-next-to-leading order in perturbative quantum chromodynamics. The impact of the measurements on the parton distribution functions and the strong coupling constant at the mass of the Z boson is investigated, yielding a value of $\alpha_S(m_Z) = 0.1179 \pm 0.0019$.

Submitted to the European Physical Journal C

1 Introduction

The production of jets in high-energy proton-proton (pp) collisions provides an important experimental input for the determination of the proton structure in terms of parton distribution functions (PDFs), and for the study of the strong force described by quantum chromodynamics (QCD). In conjunction with deep-inelastic $e^\pm p$ scattering (DIS) measurements [1, 2], which strongly constrain the quark PDFs, jet data from pp collisions at the LHC provide sensitivity to the gluon content and allow the running of the strong coupling constant α_s to be probed over a wide range of momentum scales. Recent progress made in calculating predictions for these processes at next-to-next-to-leading order (NNLO) accuracy [3, 4] in perturbative QCD (pQCD) underscores the need for precise experimental data up to the highest accessible energies.

Dijet observables are particularly well-suited for this purpose owing to the abundant production of jets in hadron-induced processes across a large phase space, which makes it possible to perform high-precision multi-differential measurements. Such measurements performed at the LHC include a triple-differential (3D) dijet measurement at a center-of-mass energy $\sqrt{s} = 8$ TeV [5] using jets reconstructed with the anti- k_T clustering algorithm [6, 7] with a distance parameter $R = 0.7$, and several double-differential (2D) measurements at 7 and 13 TeV [8–12] for anti- k_T jets with $R = 0.4, 0.6, \text{ or } 0.7$.

In this article, measurements of the dijet production cross section in pp collisions at $\sqrt{s} = 13$ TeV from the CMS Collaboration are presented, using anti- k_T jets for two values of the distance parameter, $R = 0.4$ and 0.8 . Both 2D and 3D measurements are performed as a function of the kinematic properties of the two jets with the highest transverse momenta (p_T) in the event.

In the 2D case, the cross section is measured as a function of the largest absolute rapidity $|y|_{\max}$ of the two jets and the invariant mass $m_{1,2}$ of the dijet system. For the 3D measurements, two angular observables are considered: the dijet rapidity separation $y^* = |y_1 - y_2|/2$ and the total boost of the dijet system $y_b = |y_1 + y_2|/2$, where y_1 and y_2 indicate the rapidities of the jets. The measurements are performed as a function of y^* , y_b , and $m_{1,2}$, and alternatively as a function of y^* , y_b , and the average p_T of the two jets, $\langle p_T \rangle_{1,2}$.

The 2D and 3D measurements cover a largely overlapping phase space. However, each of the two presents different experimental advantages stemming from the difference in the information content of the respective observables. The 2D measurement features a more inclusive rapidity binning, leading to an increased statistical precision and a larger accessible range in $m_{1,2}$. The use of two angular observables for the 3D measurement provides additional information on the dijet topology, at the expense of a reduced reach in $m_{1,2}$. Moreover, the variables y^* and y_b encode the dependence on the partonic scattering angle in the laboratory frame and the imbalance in the initial-state parton momenta, respectively. This is advantageous for comparisons to fixed-order pQCD predictions, which are obtained by convolving the partonic scattering cross sections and the PDFs.

This article is organized as follows. A brief description of the CMS detector is given in Section 2. Section 3 presents the samples of recorded and simulated events used for the measurement. In Section 4, the reconstruction of the event content is described, and the selection criteria applied to events entering this analysis are given. Sections 5 and 6 detail the measurement of the 2D and 3D dijet cross sections using the reconstructed jets, and the unfolding of the resulting spectra to correct for detector effects, respectively. The different sources of experimental uncertainty in the measurement are outlined in Section 7. The measurements are compared to fixed-order predictions obtained at NNLO accuracy in pQCD, which are discussed in Section 8. A comparison of the measurements to the predictions obtained for several global PDF sets is presented in

Section 9. In Section 10, the impact of including the present measurements in determinations of PDFs and the strong coupling constant at the scale of the Z boson mass, $\alpha_S(m_Z)$, is investigated. Finally, a summary of the main findings is given in Section 11.

Tabulated results are provided in the HEPData record for this analysis [13].

2 The CMS detector

The central feature of the CMS apparatus is a superconducting solenoid of 6 m internal diameter, providing a magnetic field of 3.8 T. Within the solenoid volume are a silicon pixel and strip tracker, a lead tungstate crystal electromagnetic calorimeter (ECAL), and a brass and scintillator hadron calorimeter (HCAL), each composed of a barrel and two endcap sections. Forward calorimeters extend the pseudorapidity (η) coverage provided by the barrel and endcap detectors. Muons are detected in gas-ionization chambers embedded in the steel flux-return yoke outside the solenoid.

Events of interest are selected using a two-tiered trigger system [14]. The first level, composed of custom hardware processors, uses information from the calorimeters and muon detectors to select events at a rate of around 100 kHz within a fixed latency of about 4 μ s [15]. The second level, known as the high-level trigger (HLT), consists of a processor farm running a compact version of the full event reconstruction software, optimized for fast processing, and reduces the event rate to around 1 kHz before data storage.

A more detailed description of the CMS detector, together with a definition of the coordinate system used and the relevant kinematic variables, can be found in Ref. [16].

3 Data and simulated samples

The measurements presented in this article are based on pp collision data recorded by the CMS detector in 2016 at $\sqrt{s} = 13$ TeV, corresponding to an integrated luminosity of up to 36.3 fb⁻¹. Collision events containing jets are identified during data taking by dedicated trigger algorithms. Owing to the stringent timing constraints, jets at the HLT are clustered from particle candidates reconstructed using a simplified procedure, as compared to the full offline reconstruction.

The integrated luminosity recorded by the available jet-related triggers is given in Table 1. Several sets of triggers are deployed, which require the presence of at least one jet (two jets) with a p_T (average p_T) above certain predefined thresholds. While distinct sets of single-jet triggers are deployed for anti- k_T jets with distance parameters of $R = 0.4$ and 0.8, only the former are used for the dijet triggers. The integrated luminosity delivered by each of these triggers depends on the total time period during which it was deployed. In addition, low-threshold triggers are prescaled by a factor that is continually adjusted during data taking to optimize the data acquisition rate, resulting in lower effective integrated luminosities.

To study the impact of the detector response on the measurement, samples of simulated events produced using Monte Carlo (MC) event generators are used. Events are generated at leading order (LO) in pQCD using PYTHIA 8 [17] (version 212) with the CUETP8M1 tune [18]. The matrix element calculation is matched to the parton shower and takes multi-parton interactions and hadronization effects into account. An alternative LO sample, generated using the MADGRAPH5_aMC@NLO program [19] (version 2.2.2) and interfaced with PYTHIA for the simulation of parton showering and hadronization, is used to estimate the dependence of results on the

Table 1: Overview of the single-jet (dijet) triggers deployed for the different p_T ($\langle p_T \rangle$) thresholds at the HLT, and the corresponding integrated luminosities.

	Trigger threshold (GeV)									
	40	60	80	140	200	260	320	400	450	500
Trigger set	Int. luminosity (pb^{-1})					Int. luminosity (fb^{-1})				
Single-jet $R = 0.4$	0.3	0.7	2.8	24.2	103.6	0.6	1.8	5.2	36.3	36.3
Single-jet $R = 0.8$	0.05	0.3	1.0	10.1	85.8	0.5	1.5	4.6	33.5	33.5
Dijet $R = 0.4$	0.1	1.7	4.2	27.9	140.2	0.5	3.0	9.1	—	29.6

simulation model.

To simulate contributions from additional pp collisions (pileup), the particles emerging from the high-energy scattering are overlaid with simulated minimum-bias events and propagated through a full simulation of the CMS detector modeled using the GEANT4 package [20]. The resulting signals are then processed using the same reconstruction techniques used for collision data. Differences between the simulated and measured pileup activity are accounted for using a global reweighting of simulated events based on the mean number of pileup interactions determined in data based on an estimated inelastic pp collision cross section of 69.2 mb. This number is obtained using the pileup counting method described in the inelastic cross section measurement [21]. About 23 pileup interactions occurred for each proton bunch collision during the 2016 data taking [22].

4 Event reconstruction and selection

A global description of collision events is achieved following the particle-flow approach [23], which aims to identify and measure the kinematic properties of each individual particle emerging from the collision using an optimized combination of information from the various elements of the CMS detector.

The trajectories of charged particles, as well as their originating pp interaction vertices are reconstructed from hits in the inner tracking detectors. The primary vertex is taken to be the vertex corresponding to the hardest scattering in the event, evaluated using tracking information alone, as described in Section 9.4.1 of Ref. [24].

Muons are identified as particle tracks in the inner detector layers that are compatible with either a track or several hits in the muon system, and are associated with calorimeter deposits consistent with the muon hypothesis. The muon four-momentum is determined by fitting the muon trajectory using information from both the inner tracker and the muon system.

Photons are identified as ECAL energy clusters not linked to the extrapolation of any charged-particle track to the ECAL. Electrons are identified by linking a primary charged-particle track to potential energy deposits in the ECAL. The resulting energy clusters are required to be spatially compatible with the extrapolated track to the ECAL, or consistent with bremsstrahlung photons emitted in the tracker material. While for photons the energy is obtained directly from the ECAL measurement, the electron energy is determined from a combination of the track momentum at the primary interaction vertex and the associated ECAL clusters.

Charged hadrons are identified as particle tracks not identified as electrons or muons, and neutral hadrons are identified as HCAL energy clusters not linked to any charged-hadron tra-

jectory, or as a combined ECAL and HCAL energy excess with respect to the expected charged hadron energy deposit. The energy of charged hadrons is determined by combining the track momentum and the corresponding ECAL and HCAL energies, corrected for the response function of the calorimeters to hadronic showers. The energy of neutral hadrons is obtained from the corresponding corrected ECAL and HCAL energies.

For each event, jets are clustered from the reconstructed particle candidates using the infrared and collinear-safe anti- k_T algorithm [6, 7] with distance parameters of $R = 0.4$ and 0.8 . The jet momentum is determined as the vector sum of all particle momenta in the jet, and is found from simulation to be, on average, within 5–10% of the true momentum over the entire p_T range and detector acceptance used in the analysis. To mitigate the effect of pileup, which can contribute additional tracks and calorimetric energy depositions to the jet momentum, charged particles identified as originating from pileup vertices are discarded and an offset correction [25] is applied to account for the remaining contributions.

Jet energy corrections [26] are derived from simulation studies so that the average energy of reconstructed jets becomes identical to that of particle-level jets. The latter are defined as jets clustered from all stable particles produced in the collision, excluding neutrinos. In situ measurements of the momentum balance in dijet, photon + jet, Z + jet, and multijet events are used to account for any residual differences in the jet energy scale (JES) between data and simulation. The jet energy resolution (JER) typically amounts to 15–20% at 30 GeV, 10% at 100 GeV, and 5% at 1 TeV [26]. It is measured in data using similar jet balancing approaches as for the JES, and residual differences between data and simulation are corrected by smearing the p_T of simulated jets accordingly. Additional selection criteria [27] are applied to each jet to remove jets potentially dominated by spurious contributions from various subdetector components or reconstruction failures.

The missing p_T is computed as the negative vector sum of the p_T of all the particle-flow candidates in an event, and its magnitude is denoted as p_T^{miss} [28]. The p_T^{miss} is modified to account for corrections to the energies of the reconstructed jets in the event. Anomalous high- p_T^{miss} events can be due to reconstruction failures, detector malfunctions, or noncollision backgrounds. Such events are rejected by event filters that are designed to identify more than 85–90% of the spurious high- p_T^{miss} events with a misidentification rate of less than 0.1% [28].

Events entering the 2D cross section measurements for both $R = 0.4$ and 0.8 are required to have been accepted by at least one single-jet trigger path operating on jets with the same distance parameter. For the 3D measurements, the dijet triggers are used on account of their lower overall prescale values.

To guarantee a high reconstruction efficiency at the trigger level, trigger paths with different thresholds are assigned to mutually exclusive phase space regions. These are determined for single-jet (dijet) triggers based on measurements of the trigger efficiency as a function of the leading jet p_T (average p_T of the two leading jets), requiring the trigger efficiency to remain above 99.5% in each region.

During the 2016 data taking, a gradual shift in the timing of the inputs of the ECAL first-level trigger in the region defined by $|\eta| > 2.0$ caused the trigger signal to be incorrectly associated to the previous bunch crossing (“prefiring”), leading to a specific trigger inefficiency. For events containing a jet with a p_T larger than ≈ 100 GeV, the efficiency loss in the region $2.5 < |\eta| < 3.0$ is ≈ 10 –20%, depending on p_T , η , and time. Correction factors were computed from data and applied to the acceptance evaluated from simulation.

Further selection criteria are applied to events passing the trigger selection, based on the kine-

matic properties of the two p_T -leading jets: the transverse momentum of the p_T -leading (sub-leading) jet is required to be above 100 (50) GeV, and the absolute rapidity of both jets is required to be less than 3.0.

5 Cross section measurement

The dijet production cross section is measured both double- and triple-differentially for anti- k_T jets with distance parameters of $R = 0.4$ and 0.8 in terms of the properties of the system formed by the two p_T -leading jets. The 2D spectra are reconstructed as a function of $m_{1,2}$ in five rapidity regions defined in terms of the variable $|y|_{\max} = |y_{\max}|$, where y_{\max} corresponds to the rapidity of the jet closer to the beam line (outermost jet), and is given by

$$y_{\max} = \text{sign}(|\max(y_1, y_2)| - |\min(y_1, y_2)|) \max(|y_1|, |y_2|). \quad (1)$$

In the 3D case, the cross section is measured as a function of $m_{1,2}$ and $\langle p_T \rangle_{1,2}$ in 15 rapidity regions, defined in terms of the dijet rapidity separation y^* and the total boost y_b of the dijet system, as given by

$$y^* = \frac{1}{2}|y_1 - y_2|, \quad y_b = \frac{1}{2}|y_1 + y_2|. \quad (2)$$

The variables $m_{1,2}$ and $\langle p_T \rangle_{1,2}$ are obtained as

$$m_{1,2} = \sqrt{(E_1 + E_2)^2 - (\vec{p}_1 + \vec{p}_2)^2}, \quad \langle p_T \rangle_{1,2} = \frac{1}{2}(p_{T,1} + p_{T,2}), \quad (3)$$

where the subscripts 1 and 2 refer to the p_T -leading and p_T -subleading jets, respectively.

The differential dijet spectra are reconstructed from the effective event yield N_{eff} in bins of the chosen observables, normalized to the integrated luminosity \mathcal{L}_{int} . The effective event yield is calculated from the raw event yield, taking into account the selection efficiency and subtracting background contributions. In addition, events that enter the measurement are weighted according to the prescale factor of the trigger path assigned to the corresponding phase space region.

The 2D cross section is obtained as a function of y_{\max} and $m_{1,2}$ as

$$\frac{d^2\sigma}{dy_{\max} dm_{1,2}} = \frac{1}{\mathcal{L}_{\text{int}}} \frac{N_{\text{eff}}}{(2 \Delta|y|_{\max}) \Delta m_{1,2}}. \quad (4)$$

Here, $\Delta|y|_{\max}$ and $\Delta m_{1,2}$ denote the width of the bins in the respective quantities. The measurement is performed in five rapidity bins of equal size within $0 < |y|_{\max} < 2.5$ and covers an invariant mass range of $249 < m_{1,2} < 10\,050$ GeV. The measurement boundaries are chosen starting from a preliminary binning determined using simulated samples based on the expected experimental resolution in $m_{1,2}$, and discarding bins at low $m_{1,2}$ that do not meet the minimal trigger efficiency requirement of 99.5%, and bins at high $m_{1,2}$ for which the statistical uncertainty exceeds 50%.

For the 3D measurement, the cross section is obtained as

$$\frac{d^3\sigma}{dy^* dy_b dx} = \frac{1}{\mathcal{L}_{\text{int}}} \frac{N_{\text{eff}}}{\Delta y^* \Delta y_b \Delta x}. \quad (5)$$

As in Eq. (4), the event yield is normalized to the observable bin widths Δy^* , Δy_b and Δx , where x stands for either $m_{1,2}$ or $\langle p_T \rangle_{1,2}$. Fifteen rapidity regions are investigated, covering

the range from 0 to 2.5 in each observable, as illustrated in Fig. 1. Different invariant mass and average transverse momentum regions are measured depending on the rapidity region, covering a range of $306 < m_{1,2} < 6094$ GeV and $147 < \langle p_T \rangle_{1,2} < 2702$ GeV, respectively. These ranges are obtained using an analogous procedure as for the 2D measurements.

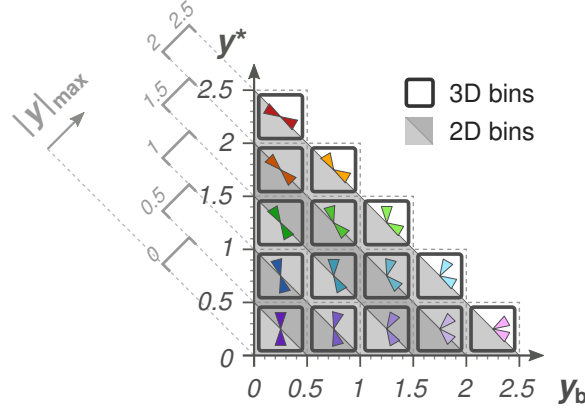


Figure 1: Illustration of the dijet rapidity phase space, highlighting the relationship between the variables used for the 2D and 3D measurements. The colored triangles are suggestive of the orientation of the two jets in the different phase space regions in the laboratory frame, assuming that the beam line runs horizontally.

6 Unfolding

Because of the finite detector resolution and other experimental effects, such as the reconstruction efficiency, the properties of reconstructed jets differ from those of jets defined at the particle level. This leads to a migration of dijet events within the phase space spanned by the observables used for the cross section measurement. To enable a direct comparison of the measured cross sections to theoretical particle-level calculations or to other measurements, the effect of these migrations is accounted for as part of a multi-dimensional unfolding procedure.

Using simulated event samples, the dijet observables of interest are computed event by event based on both the two p_T -leading reconstructed jets and the jets clustered directly from generated particles. Response matrices are constructed to reflect the probability of bin-to-bin event migrations between the particle and reconstruction levels, taking all the observables used for a measurement into account simultaneously.

The measured event distributions are unfolded using the TUNFOLD package [29], based on the simulation-derived response matrices. While no explicit regularization of the unfolded distributions is performed, large fluctuations between neighboring bins stemming from an ill-conditioned response matrix are avoided through an appropriate choice of bins. These are chosen in such a way as to ensure that the bin sizes remain at least twice as large as the resolution in these variables, and that the purity is at the level of 50% or above. The latter is defined as the fraction of reconstructed events in each bin that originate from genuine dijet events in the same bin at the particle level.

To ensure that the unfolding problem is well-posed, a larger number of bins is chosen for the reconstructed distributions than for the particle-level distributions. Moreover, because of the larger resolution and the decrease in purity at outer rapidities, a coarser particle-level binning is chosen for the two outermost $|y|_{\max}$ regions for the 2D measurements, and the corresponding nine outermost (y^*, y_b) regions for the 3D measurements. All response matrices obtained in

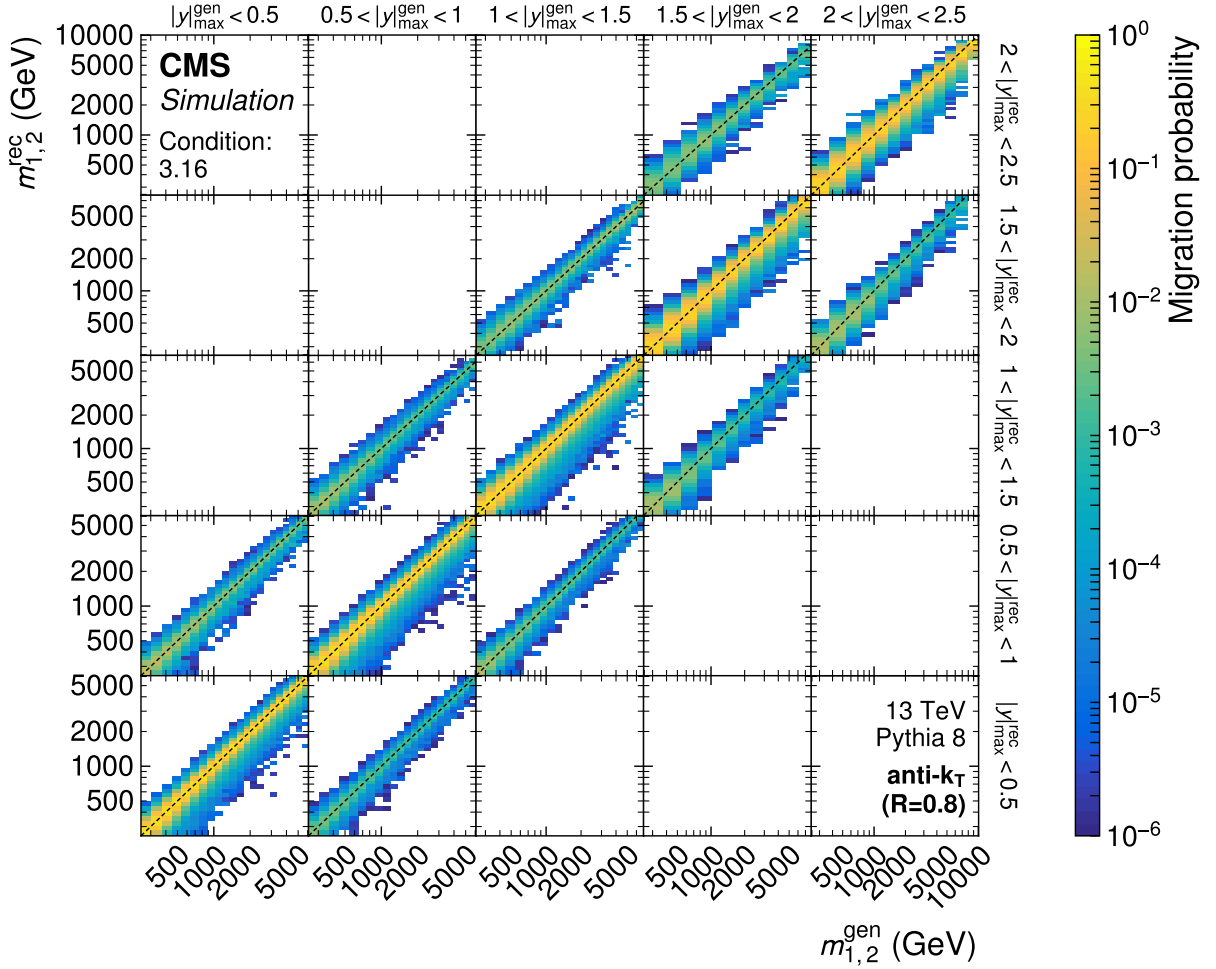


Figure 2: Response matrix for the 2D measurement as a function of $m_{1,2}$ using jets with $R = 0.8$. The entries represent the probability for a dijet event generated in the phase space region $(m_{1,2}^{\text{gen}}, |y|_{\text{max}}^{\text{gen}})$ indicated on the x axis to be reconstructed in the phase space region $(m_{1,2}^{\text{rec}}, |y|_{\text{max}}^{\text{rec}})$ indicated on the y axis. Response matrices for all other jet sizes and observables can be found in Appendix B.

this way exhibit condition numbers of ≈ 3 and are thus suitable for unfolding without regularization. The condition number is defined as the absolute value of the ratio between the largest and smallest matrix eigenvalue. Figure 2 shows the responses obtained for a representative choice of jet distance parameters and dijet observables.

Aside from event migrations within the measurement phase space, contributions to each bin from spurious jet reconstructions, pileup, changes in the p_T ordering of jets, or migrations into the phase space, are evaluated in the simulation and proportionally subtracted from the measured distributions prior to unfolding. Similarly, to correct for event losses due to the finite reconstruction efficiency, changes in the p_T ordering of jets, or migrations outside the phase space, bin-by-bin correction factors are derived from simulation and applied to the unfolded distributions.

7 Experimental uncertainties

Statistical fluctuations in the observed event counts and various systematic effects give rise to experimental uncertainties in the measured cross sections. The statistical uncertainties are calculated from the event counts in each bin assuming a Poisson distribution and the corresponding covariance matrix is propagated through the unfolding procedure to yield a full set of statistical uncertainties and correlations for the unfolded cross sections. For both the 2D and 3D measurements, the statistical uncertainties remain below 2% in most phase space regions, generally increasing to 2–5% at outer rapidities and reaching values of 20–40% at large $m_{1,2}$ or $\langle p_T \rangle_{1,2}$.

The impact of systematic effects on the cross section is generally estimated by varying experimental parameters within a ± 1 standard deviation interval around the nominal value. The relative differences to the nominal result are used to construct an asymmetric confidence interval for the unfolded cross sections in each observable bin.

Figures 3 and 4 show an overview of the main contributions to the experimental uncertainty in the dijet cross section for the 2D measurement for both values of R , and the 3D measurement as a function of $\langle p_T \rangle_{1,2}$ for $R = 0.4$, respectively. The main contributions to the systematic uncertainty are due to the determination of the JES and JER, and the luminosity. A further uncertainty results from the correction of the trigger prefiring inefficiency, and is only significant in the outer rapidity regions with contributions from jets with $|y| > 2$. Other contributions, which have an overall smaller impact on the cross section, arise as a consequence of experimental methods such as unfolding. The following sections describe the individual uncertainty contributions in more detail.

7.1 Jet energy scale uncertainty

The dominant contribution to the systematic uncertainty arises from the determination of the JES. Jets are calibrated in a multi-stage procedure to correct for experimental effects, such as contributions from pileup collisions or shifts in the jet energy due to detector or reconstruction effects. The corrections depend on the p_T and η of the jet, and lead to a total uncertainty in the energy scale of individual jets of 1–2% in the phase space considered here [30]. Since the dijet spectrum decreases exponentially as a function of $m_{1,2}$ and $\langle p_T \rangle_{1,2}$, the resulting uncertainty in the measured differential dijet cross section is amplified by this exponent. For the 2D cross sections, the JES uncertainty starts at 2–5%, reaching 30% at higher values of $m_{1,2}$. For the 3D cross section the total JES uncertainty increases with $m_{1,2}$ ($\langle p_T \rangle_{1,2}$) from about 3% up to values between 8 and 60% (40%), depending on the rapidity region.

The total JES uncertainty is composed of 22 individual contributions describing different systematic effects. These include, in roughly descending order of their impact on the cross section: the change in experimental conditions over time, the calibration of the relative and absolute JES as a function of η and p_T , the change in response for jets initiated by gluons and different quark flavors, and pileup collisions. Each contribution represents a fully correlated uncertainty across all data points and is considered to be independent of the other contributions.

7.2 Luminosity uncertainty

The uncertainty due to the integrated luminosity measurement is evaluated to be 1.2% [31] in all phase space regions and is considered to be fully correlated across all bins.

7.3 Jet energy resolution uncertainty

The effect of the finite JER on the cross section is modeled using response matrices obtained from the simulation, where the effective JER is increased by factors derived from control samples in data to account for residual differences between the detector simulation and the actual data-taking conditions. The correction of the JER is applied as part of the unfolding procedure. The JER uncertainty in the cross section is estimated by performing the unfolding with response matrices derived from alternative samples, where the jet energy was smeared by factors representing a ± 1 standard deviation shift in the JER compared to the nominal value. The resulting uncertainty values range from below 1% at central rapidities to at most 10% in the outer rapidity regions, and are considered to be correlated across all data points.

7.4 Unfolding uncertainties

A further uncertainty arises as a consequence of the limited size of the simulated samples used for deriving the response matrices as part of the unfolding procedure. These are thus subject to an intrinsic statistical uncertainty, which is propagated analytically to the unfolded cross sections. In most phase space regions, this uncertainty remains below 0.5%, reaching values of 5–10% only in a small number of bins at the highest $m_{1,2}$ or $\langle p_T \rangle_{1,2}$. As an estimate of the model dependence introduced by unfolding, the difference in the cross sections unfolded with response matrices obtained from PYTHIA 8 and MADGRAPH5_AMC@NLO is taken as an additional uncertainty, which is considered to be correlated across all data points. This uncertainty is typically at the level of 1%, rising up to at most 10% at outer rapidities and high $m_{1,2}$.

7.5 Other uncertainties

The correction applied to compensate for the trigger inefficiency due to pre-firing gives rise to an additional correlated uncertainty in the cross section. In general, this uncertainty is at the level of 1% or below, except in the outermost $|y|_{\max}$ region and the five outermost (y^*, y_b) regions, where it rises to about 10% (20%) at the upper end of the $m_{1,2}$ ($\langle p_T \rangle_{1,2}$) spectrum.

The uncertainty contribution from pileup interactions is determined by varying the total inelastic pp cross section used for reweighting the simulated samples within its associated uncertainty of 4.6%, as obtained using the pileup counting method described in Ref. [21]. The unfolding is then performed with the resulting response matrices, taking the differences between the variations and the nominal value as a fully correlated uncertainty in the unfolded cross section, which is below 1% in all phase space regions.

The normalization uncertainty in the background contribution from spurious jet reconstructions or event migrations at the phase space boundaries is estimated to be 5% and propagated through the unfolding procedure. A further contribution to the uncertainty in the unfolded cross section is due to the correction of reconstruction inefficiencies and migrations outside the measurement phase space and is estimated to be 5% of the corresponding correction factors. Each of the above contributions is considered to be fully correlated across all data points.

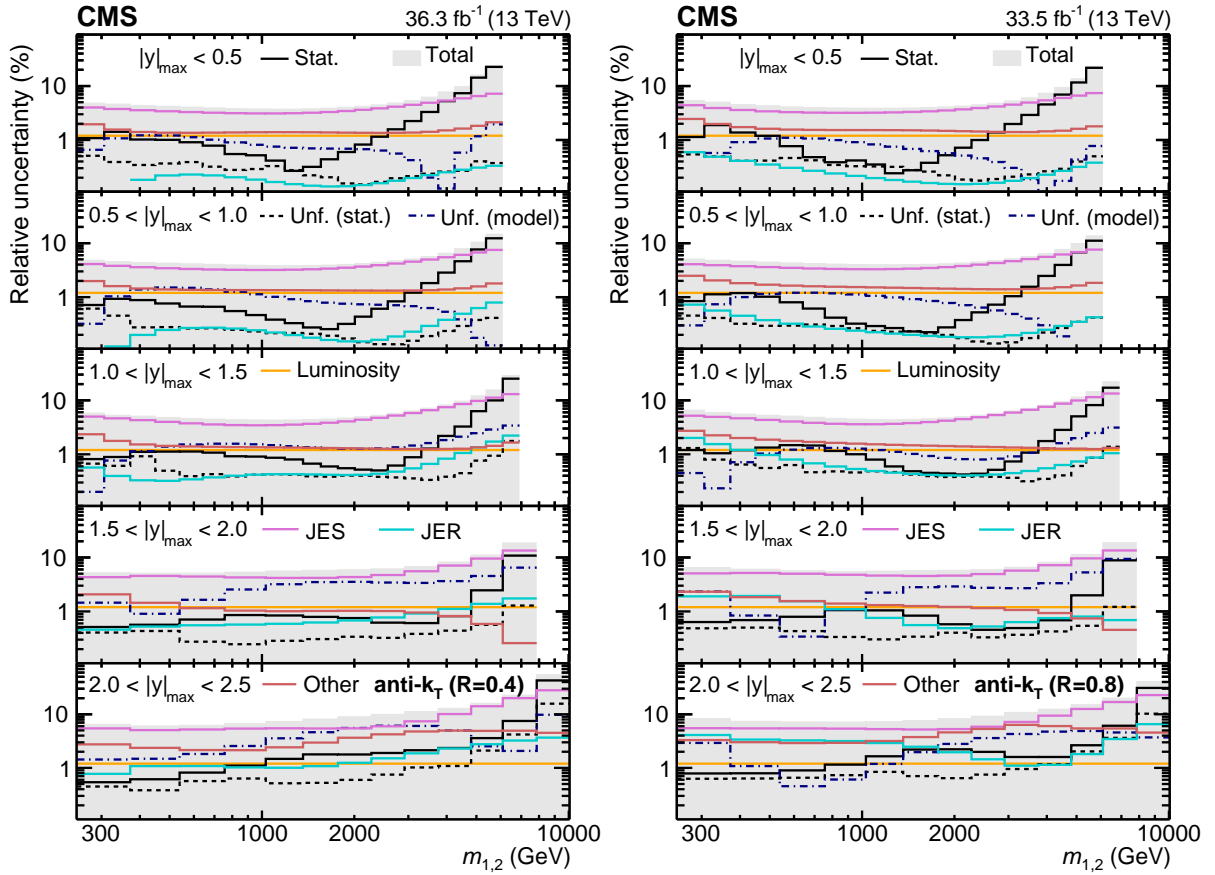


Figure 3: Breakdown of the experimental uncertainty for the 2D measurements as a function of $m_{1,2}$ using jets with $R = 0.4$ (left) and 0.8 (right). The individual components are discussed in Section 7, and the abbreviation “Unf.” refers to the unfolding uncertainties. The shaded area represents the sum in quadrature of all statistical and systematic uncertainty components.

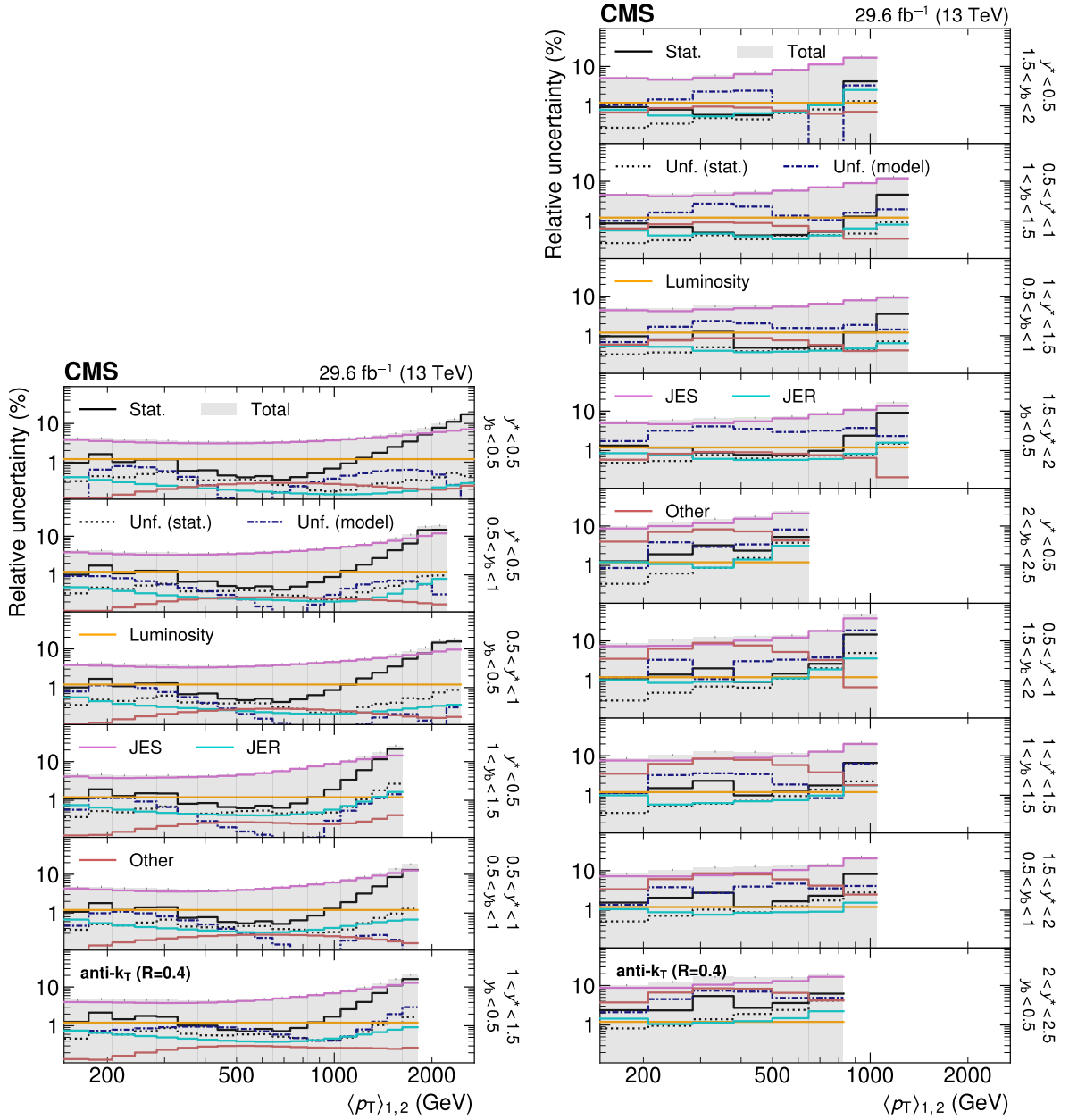


Figure 4: Breakdown of the experimental uncertainty for the 3D measurement as a function of $\langle p_T \rangle_{1,2}$ using jets with $R = 0.4$. The individual components are discussed in Section 7. The shaded area represents the sum in quadrature of all statistical and systematic uncertainty components. Similar plots for all other jet sizes and observables can be found in Appendix B.

8 Theoretical predictions

Fixed-order theoretical predictions for the 2D and 3D dijet cross sections are obtained up to NNLO accuracy in pQCD with the NNLOJET program (revision 5918) [32]. The NNLOJET program is interfaced to FASTNLO (version 2.3) [33, 34] via the APPLFAST interface (version 0.0.46) [35, 36] to provide interpolation grids that allow theoretical predictions to be obtained for arbitrary PDFs and for different values of the renormalization scale μ_R , the factorization scale μ_F , and the strong coupling constant $\alpha_S(m_Z)$, without the need to repeat the full calculation.

Following recommendations outlined in Ref. [37], $m_{1,2}$ is chosen as the central reference value for both μ_R and μ_F . To estimate the theoretical uncertainty due to missing higher-order terms in perturbation theory, the conventional recipe [38–40] of varying the μ_R and μ_F scales is applied. More precisely, the so-called scale uncertainty is derived from the envelope of the theoretical predictions obtained for the six scale variations corresponding to $(\mu_R/m_{1,2}, \mu_F/m_{1,2}) = (1/2, 1/2), (1/2, 1), (1, 1/2), (2, 1), (1, 2),$ and $(2, 2)$. As an example, Fig. 5 shows the resulting uncertainty for theoretical predictions of the 2D and 3D dijet cross sections obtained at LO, next-to-leading order (NLO), and NNLO. In most phase space regions, the NLO and NNLO scale uncertainty bands overlap, indicating good perturbative convergence. However, towards small values of $m_{1,2}$ and large rapidity separations y^* , a steep rise in the ratio of the higher-order predictions with respect to LO, referred to here as the K factors, is observed, leading to a reduced overlap and an increased scale uncertainty. For an ideal dijet event with two jets of equal p_T produced in a back-to-back configuration, the dijet invariant mass is given by $m_{1,2} = 2p_T \cosh(y^*)$. The rise in the K factors then is understood to be caused by the minimum p_T requirements imposed on the two leading jets, which at small dijet mass restrict the phase space accessible to LO processes in favor of higher-order contributions. Consequently, the cross sections for some of the low- $m_{1,2}$ bins are less well predicted by perturbation theory.

The NNLO contribution is based on the leading-color and leading-flavor-number approximation [3, 4]. Subleading-color contributions have been shown to be at the percent level at NLO and are expected to be even smaller in comparison to the leading-color result at NNLO [41]. It is worth noting, however, that in a recent investigation [42] a significant impact of subleading-color contributions was found for the NNLO prediction of the $\langle p_T \rangle_{1,2}$ -dependent 3D CMS dijet measurement at $\sqrt{s} = 8$ TeV with a jet distance parameter $R = 0.7$ [5]. The reported effect can lead to a decrease in the cross section of up to 5 for small $\langle p_T \rangle_{1,2}$ and an increase of up to 3% for large $\langle p_T \rangle_{1,2}$, which is beyond the size of the scale uncertainty at NNLO. For the CMS inclusive jet measurement at $\sqrt{s} = 13$ TeV [43] with jet distance parameters of $R = 0.4$ and 0.7 , the effect was determined to be much smaller and to be covered by scale uncertainty estimates, except towards small jet p_T for the smaller jet size. Predictions for the 2D dijet measurement performed as a function of $m_{1,2}$ and y^* at $\sqrt{s} = 7$ TeV by the ATLAS Collaboration [11] were also less affected even with $R = 0.4$. The effect on the dijet observables under examination here is not yet known. The 2D and 3D measurements presented here for two jet distance parameters, $R = 0.4$ and 0.8 , and for the two dijet observables $m_{1,2}$ and $\langle p_T \rangle_{1,2}$, provide an ideal set of measurements to further study the impact of subleading-color corrections in comparison to data.

To compare with CMS data unfolded to the particle level, the fixed-order predictions are complemented by nonperturbative (NP) correction factors c_{NP} , which are defined as the ratio between the nominal cross sections with and without multiple parton interactions (MPI) and

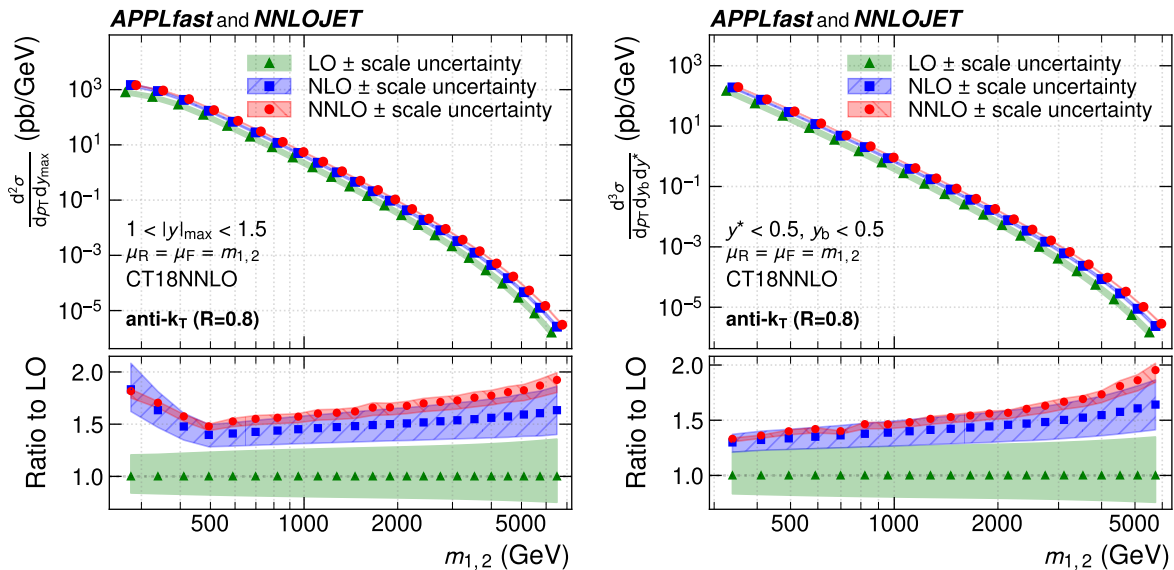


Figure 5: Theoretical predictions for the 2D (left) and 3D (right) cross sections, as a function of $m_{1,2}$, illustrated here in the rapidity regions $1.0 < |y|_{\max} < 1.5$ and $y_b < 0.5$, $y^* < 0.5$, together with the corresponding six-point scale uncertainty for $\mu_R = \mu_F = m_{1,2}$ using the CT18 NNLO PDF set. In the upper panels, the curves and symbols are slightly shifted for better visibility. The lower panels show the ratio to the respective prediction at LO. The fluctuations in the NNLO predictions are due to the limited statistical precision of the calculation.

hadronization (HAD) effects, as given by a chosen MC event generator,

$$c_{\text{NP}} = \frac{\sigma^{\text{PS+MPI+HAD}}}{\sigma^{\text{PS}}}, \quad (6)$$

where the parton shower (PS) is considered to be a perturbative component.

The model dependence of the NP corrections is evaluated by comparing results from several MC event generators. Leading-order particle-level predictions are obtained from PYTHIA (version 8.240), using the tunes CUETP8M1 [18] and CUETP8M2T4 [44], and HERWIG++ [45] (version 2.7.1) using the EE5C tune [46]. These generators are interfaced to POWHEG [47–50] (version 2J V2_Mar2016) to provide NLO predictions. An additional set of predictions is obtained from HERWIG 7 [51] (version 7.2.2) with the CH3 tune [52] at both LO and NLO.

To mitigate statistical fluctuations, the corrections are parametrized by a smooth function $f(x) = a/x^b + c$, where x is either $m_{1,2}$ or $\langle p_T \rangle_{1,2}$. The parameters a , b , and c are obtained in a least-squares fit to the binwise correction factors c_{NP} obtained from Eq. (6) in each rapidity region. For a number of low- $m_{1,2}$ bins, where the phase space is constrained by the minimum p_T requirements on the two leading jets, the value of c_{NP} is taken directly as the correction factor. The final correction factor in each bin is obtained as the midpoint between the largest and smallest value of c_{NP} obtained across all MC configurations, and half the difference between the largest and smallest value is assigned as an uncertainty.

The resulting NP corrections are illustrated in Fig. 6. For jets with $R = 0.4$, the contributions from hadronization and MPI largely cancel, leading to NP corrections compatible with unity within their uncertainty. In contrast, the MPI contribution dominates for jets with $R = 0.8$, resulting in significantly larger NP corrections of $\approx 20\%$ at low values of $m_{1,2}$. The size of the uncertainty is similar for both jet sizes.

It is also observed that the NP corrections obtained with PYTHIA 8 are in general larger than those from HERWIG++ or HERWIG 7, such that this difference is the dominant contribution to the NP correction uncertainty. While some dependence on the tune is observed when comparing the predictions from CUETP8M1 and CUETP8M2T4, the impact is typically small. In most cases, the values obtained at NLO are seen to be comparable to those obtained at LO from the same generator, with the notable exception of HERWIG++, where the NLO result obtained using POWHEG is consistently higher than the LO result.

For jet transverse momenta in the TeV range, electroweak contributions to the differential dijet cross section become important and must be considered in addition to the NNLO pQCD calculation [53]. These effects, which arise from the virtual exchange of soft or collinear W or Z bosons, are accounted for by applying a multiplicative correction factor to the pQCD prediction. As shown in Fig. 7, these factors exhibit a strong dependence on the rapidity and p_T of the jets. Particularly at small $|y|_{\max}$ or y^* , the electroweak correction reaches 10–20% for dijet masses beyond 5 TeV, where experimental uncertainties become large as well. The uncertainty on this correction is therefore considered to be negligible with respect to other large uncertainties.

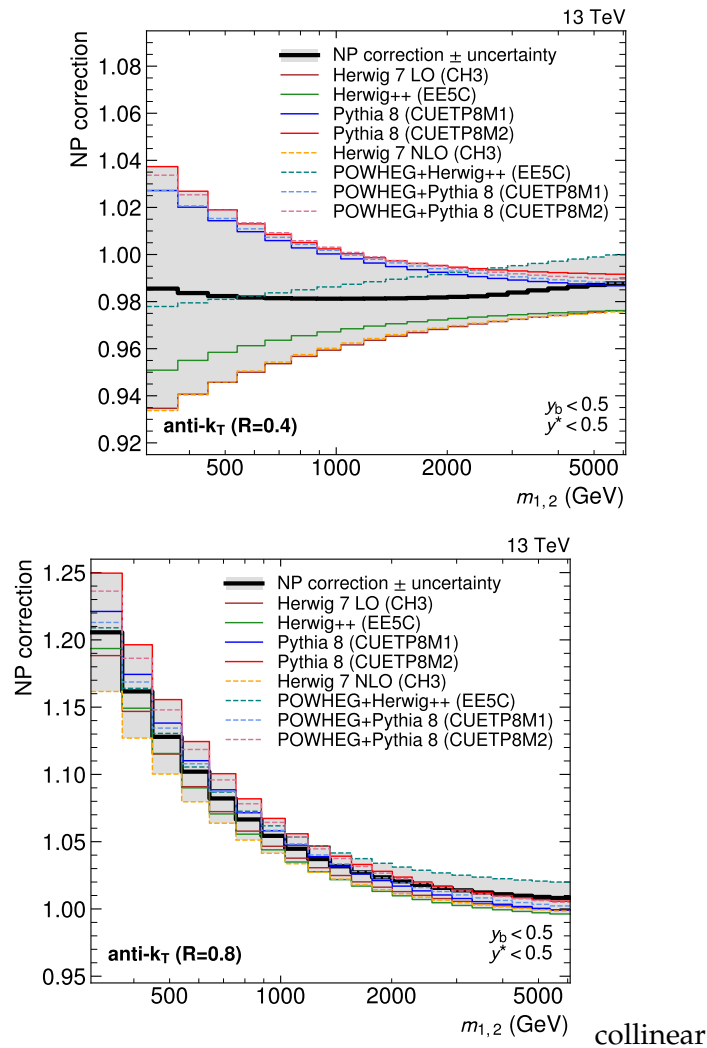


Figure 6: Nonperturbative correction factors obtained for jets with $R = 0.4$ (left) and 0.8 (right) as a function of $m_{1,2}$, illustrated here in the rapidity region ($y_b < 0.5$, $y^* < 0.5$). Individual correction factors are first derived from simulation using eight different MC configurations. The largest and smallest value obtained in each observable is then used to define the final correction factor and its associated uncertainty. The correction values are larger for jets with $R = 0.8$, increasing to over 20% in the lowest $m_{1,2}$ bin.

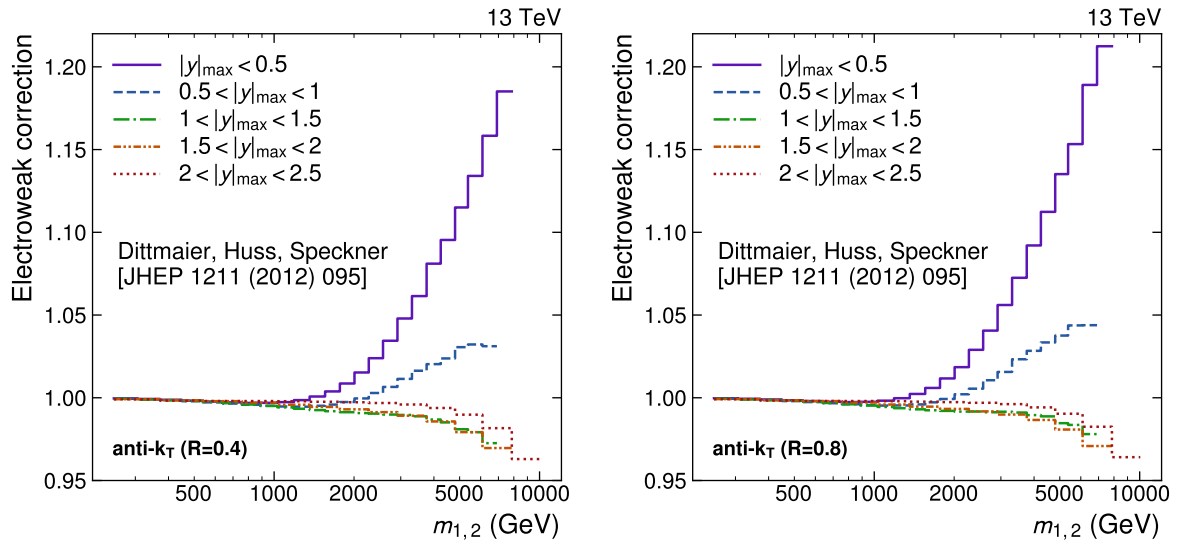


Figure 7: Electroweak correction factors obtained for jets with $R = 0.4$ (left) and 0.8 (right) as a function of $m_{1,2}$ in the five different $|y|_{\max}$ regions. The corrections depend strongly on the kinematic properties of the jets and are observed to be largest at central rapidities for $m_{1,2} > 1$ TeV.

9 Comparison to theory

An overview of the unfolded cross sections obtained for the 2D and 3D measurements and the corresponding fixed-order theoretical predictions at NNLO, complemented by NP and electroweak corrections, is presented in Fig. 8. For a more detailed comparison, ratios of the measured cross sections to the theoretical predictions are shown in Figs. 9 and 10.

The theoretical predictions are obtained using recent NNLO PDF sets available via the LHAPDF [54] library (version 6.3.0), namely ABMP16 [55], CT18 [56], MSHT20 [57], and NNPDF3.1 [58]. All PDF sets are derived in global fits to data from multiple experiments while fixing the value of the strong coupling constant $\alpha_S(m_Z)$ to 0.118, except for ABMP16, where $\alpha_S(m_Z) = 0.1147$ is determined in the fit together with all other parameters. The uncertainties in the cross section predictions due to the PDFs are calculated as 68% confidence intervals following the prescriptions given in the respective references. The PDF uncertainty bands shown in Fig. 10 are obtained using the CT18 PDF set and do not account for the finite precision of $\alpha_S(m_Z)$.

The predictions for different PDFs are generally in agreement with each other within the PDF uncertainties, except for the AMBP16 PDF, for which the predicted cross sections are generally smaller than those for other PDFs. At large $m_{1,2}$ or $\langle p_T \rangle_{1,2}$, the predictions obtained for the different PDF sets show a diverging trend, while still remaining compatible within the PDF uncertainties.

The level of agreement between the theoretical predictions and the data is observed to be good in most phase space regions, with some deviations at the lower ends of the spectra and in the outer rapidity regions. In general, the theoretical predictions for $R = 0.8$ are observed to provide a better description of the data than for $R = 0.4$, which is consistent with past observations [43, 59–62].

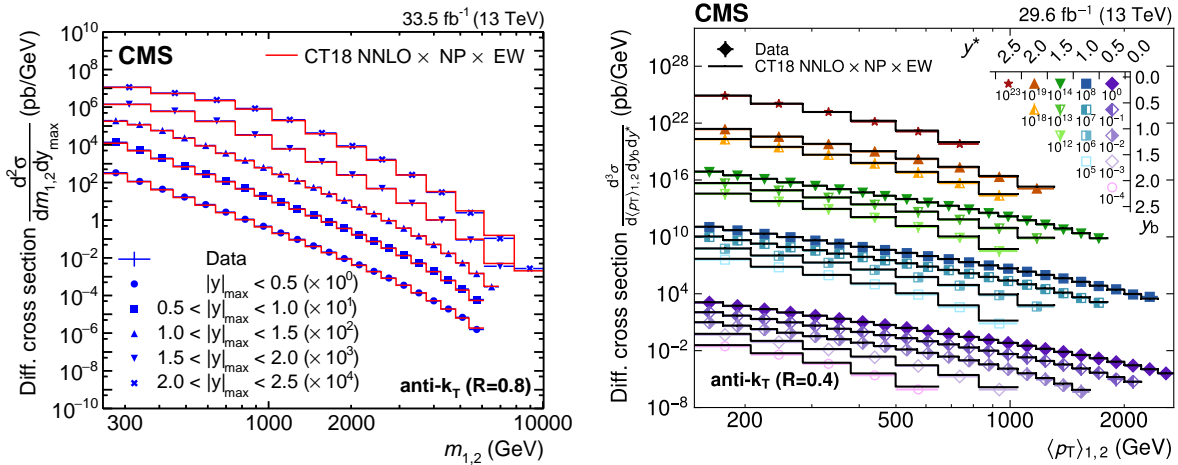


Figure 8: Differential dijet cross sections, illustrated here for the 2D measurement as a function of $m_{1,2}$ using jets with $R = 0.8$ (left), and the 3D measurement as a function of $\langle p_T \rangle_{1,2}$ using jets with $R = 0.4$ (right). The markers and lines indicate the measured unfolded cross sections and the corresponding NNLO predictions, respectively. For better visibility, the values are scaled by a factor depending on the rapidity region, as indicated in the legend. Analogous plots for all other jet sizes and observables can be found in Appendix B.

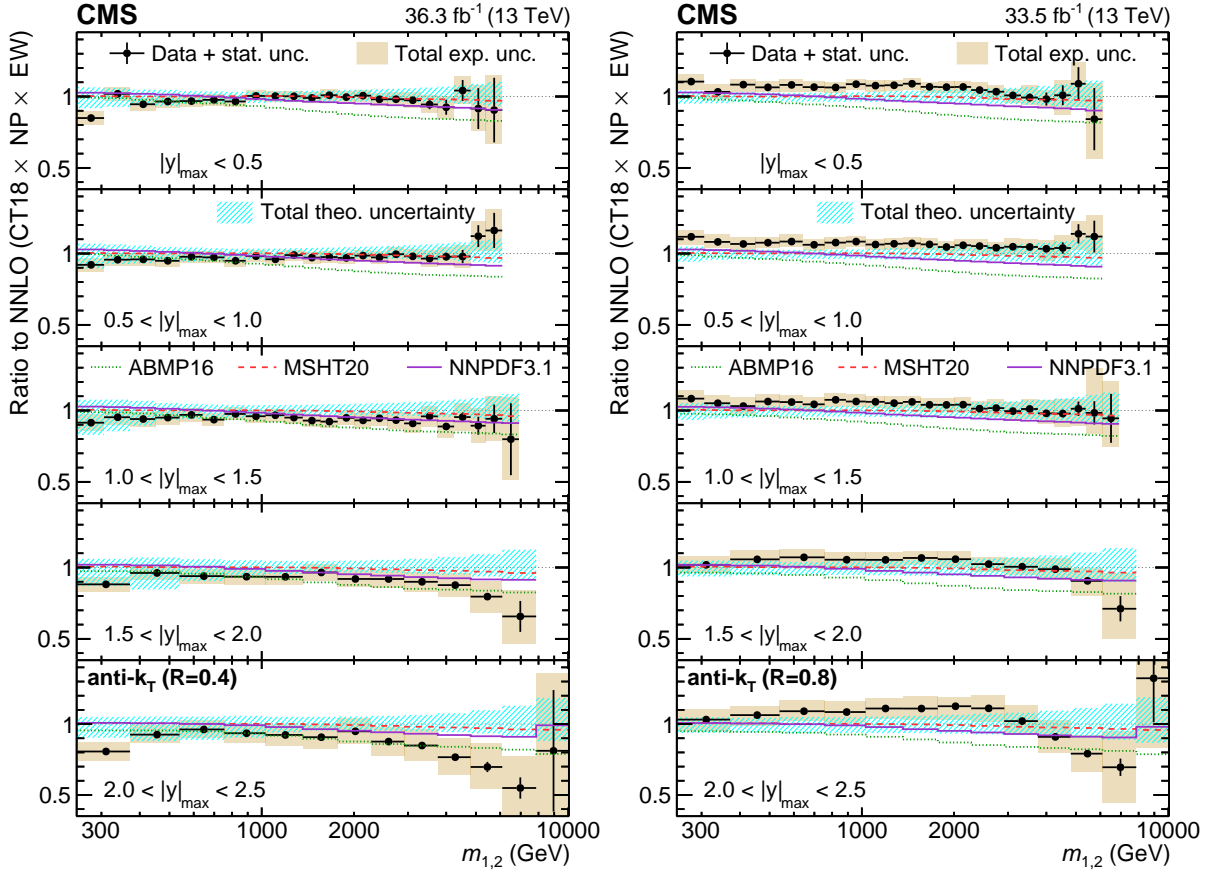


Figure 9: Comparison of the 2D dijet cross section as a function of $m_{1,2}$ to fixed-order theoretical calculations at NNLO, using jets with $R = 0.4$ (left) and 0.8 (right). Shown are the ratios of the measured cross sections (markers) to the predictions obtained using the CT18 NNLO PDF set. The error bars and shaded yellow regions indicate the statistical and the total experimental uncertainties of the data, respectively, and the hatched teal band indicates the sum in quadrature of the PDF, NP, and scale uncertainties. Alternative theoretical predictions obtained using other global PDF sets are shown as colored lines. Similar plots for the individual rapidity regions can be found in Appendix B.

10 The QCD analysis

To evaluate the impact of the present measurements on determinations of the proton PDFs and the strong coupling constant, a QCD analysis is performed following the approach taken by earlier HERAPDF analyses [1, 2, 63]. The data used in the QCD analysis comprise DIS measurements [1, 2] obtained in $e^\pm p$ collisions at the HERA collider experiments H1 and ZEUS as a function of the momentum transfer Q^2 , supplemented by the present measurements of the dijet cross section.

The HERA measurements correspond to charged-current (CC) DIS data collected in $e^- p$ and $e^+ p$ collisions at a proton beam energy of $E_p = 920$ GeV, and neutral-current (NC) DIS data collected in $e^+ p$ collisions at proton beam energies of $E_p = 460, 575, 820,$ and 920 GeV. Only data points with Q^2 values above a threshold $Q_{\min}^2 = 10$ GeV² are included, to ensure a good description of the measurements by the theoretical predictions.

It is well known that fixed-order predictions work most reliably for inclusive observables, i.e., where the phase space for QCD radiation is not restricted. Such restrictions—as for example

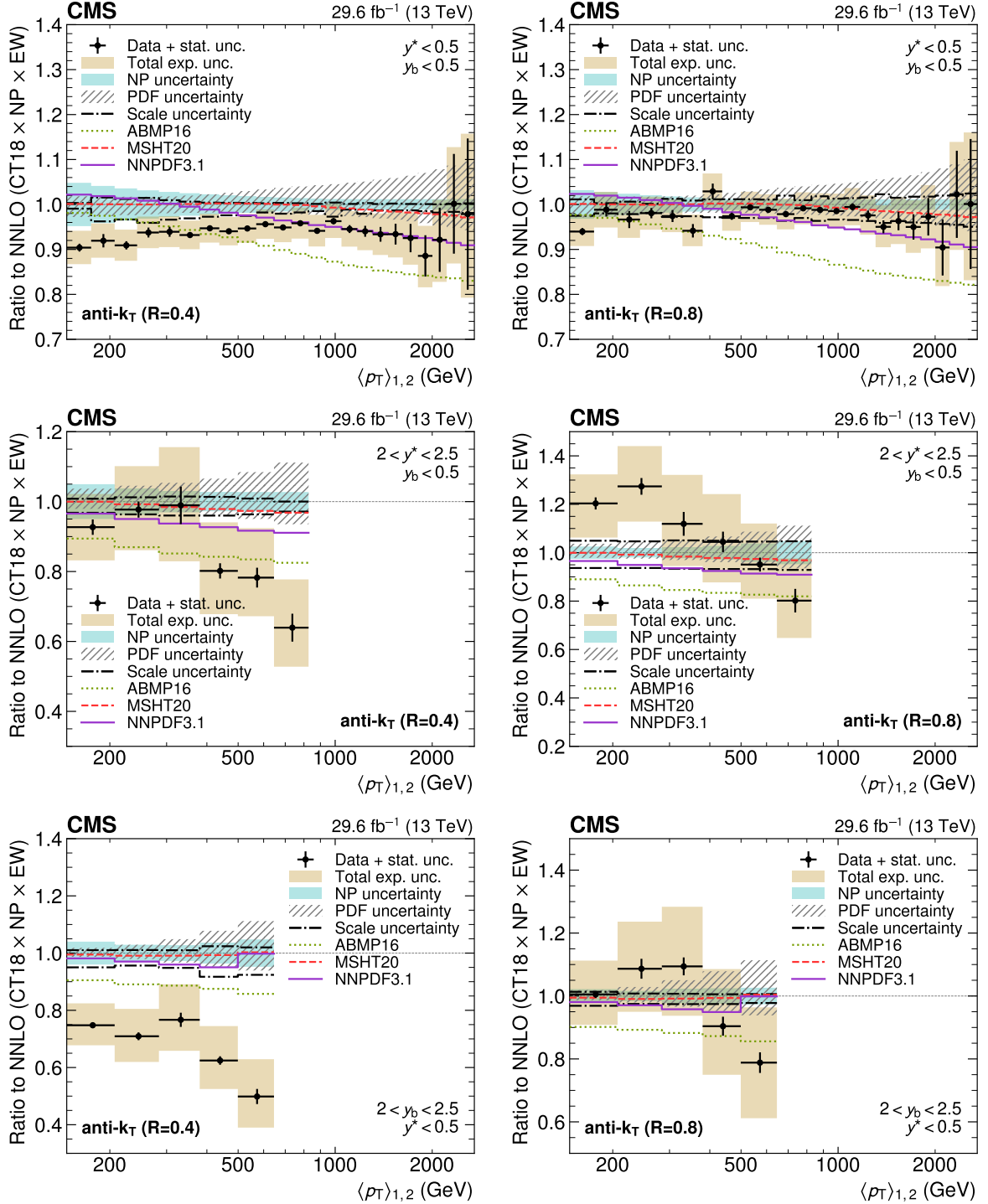


Figure 10: Comparison of the 3D dijet cross section for jets with $R = 0.4$ (left) and 0.8 (right) as a function of $\langle p_{T,1,2} \rangle$ to fixed-order theoretical calculations at NNLO, shown here for three out of the total of 15 rapidity regions. The data points and predictions for alternative PDFs are analogous to those in Fig. 9. In addition, the separate contributions to the theory uncertainty due to the CT18 PDFs, NP corrections, and six-point scale variations are shown explicitly. Similar plots for all rapidity regions and observables can be found in Appendix B.

the choice of a small distance parameter R for jet clustering—introduce disparities in the cancellation of singularities between real emissions and virtual corrections, leading to large loga-

rithmic terms that have a negative impact on the perturbative convergence and would require resummation [64]. Moreover, as discussed in Section 8, there are indications that subleading-color corrections might have a smaller impact for larger values of R , and for $m_{1,2}$ as compared to $\langle p_T \rangle_{1,2}$. Thus, to profit most from the available predictions at NNLO, only the dijet cross sections as a function of $m_{1,2}$ for the larger value of $R = 0.8$ are used in the QCD analysis.

Theoretical predictions for the dijet cross sections are obtained from NNLOJET and FASTNLO as interpolation grids at NNLO accuracy, taking into account the full dependence of the NNLO cross sections on the PDFs, the strong coupling constant, μ_R , and μ_F . Following Ref. [3], the dijet invariant mass $m_{1,2}$ is chosen as the central value for both μ_R and μ_F . The cross sections are corrected additionally for NP and electroweak effects as described in Section 8.

Simultaneous determinations of PDFs and the strong coupling constant at the scale of the Z boson mass, $\alpha_S(m_Z)$, are performed with the xFITTER program (version 2.0.1) [65, 66], using the HERA data together with either the 2D or 3D dijet cross sections as inputs. Access to the theoretical predictions for the dijet cross sections is provided by FASTNLO. The evolution of PDFs following the DGLAP equations [67–69] is performed using the QCDNUM package (version 17-01/15) [70]. Contributions from heavy quarks are treated in the Thorne–Roberts optimal variable flavor number scheme (RTOPT) [71–73], with the masses of the charm and bottom quarks set to $m_c = 1.43$ GeV and $m_b = 4.5$ GeV, respectively.

In the HERAPDF approach, the proton structure is expressed in terms of the gluon distribution $g(x)$, the up and down valence quark distributions $u_v(x)$ and $d_v(x)$, and the up- and down-type sea antiquark distributions $\bar{U}(x)$ and $\bar{D}(x)$. For each of these distributions f , the dependence on the proton momentum fraction x carried by a parton is parametrized at a starting scale $\mu_{F,0}^2 = 1.9$ GeV² as

$$xf(x, \mu_{F,0}^2) = A_f x^{B_f} (1-x)^{C_f} (1 + D_f x + E_f x^2). \quad (7)$$

The overall normalization of the PDFs is given by the A parameters, with A_{u_v} , A_{d_v} , and A_g being constrained by the quark number and momentum sum rules. The B and C parameters control the shape of the distribution as x approaches the edges of its domain at 0 and 1, respectively. The D and E parameters represent additional degrees of freedom related to the functional forms.

The sea quark contributions are given by $\bar{U}(x) = \bar{u}(x)$ and $\bar{D}(x) = \bar{d}(x) + \bar{s}(x)$, where $\bar{u}(x)$, $\bar{d}(x)$, and $\bar{s}(x)$ refer to the distribution of up, down, and strange antiquarks, respectively. A fixed overall normalization ratio is imposed by the requirement $A_{\bar{U}} = A_{\bar{D}}(1 - f_s)$, where the strangeness fraction is given by $f_s = \bar{s}/(\bar{s} + \bar{d})$ and set to 0.4 following Ref. [2]. To enforce a similar behavior of the quark sea as $x \rightarrow 0$, the requirement $B_{\bar{U}} = B_{\bar{D}}$ is imposed. The total sea quark distribution is defined as $\Sigma(x) = 2(\bar{U}(x) + \bar{D}(x))$.

The above constraints result in a total of ten A , B , and C parameters whose values are determined during the fit procedure. Additional D and E parameters are included where it is found that these lead to an improved fit quality in terms of the total χ^2 value, following the procedure outlined in Ref. [2]. Starting from the initial parametrization with no additional parameters, the change in χ^2 resulting from the inclusion of any of the remaining D and E parameters in the fit is evaluated. The parameter resulting in the largest decrease in χ^2 is added to the parametrization, and the procedure is repeated until no further significant improvement is observed. The final parametrization obtained in this way for the fits including the CMS dijet measurements is

given by:

$$\begin{aligned}
x g(x, \mu_{F,0}^2) &= A_g x^{B_g} (1-x)^{C_g}, \\
x u_v(x, \mu_{F,0}^2) &= A_{u_v} x^{B_{u_v}} (1-x)^{C_{u_v}} (1 + D_{u_v} x + E_{u_v} x^2), \\
x d_v(x, \mu_{F,0}^2) &= A_{d_v} x^{B_{d_v}} (1-x)^{C_{d_v}}, \\
x \bar{U}(x, \mu_{F,0}^2) &= A_{\bar{U}} x^{B_{\bar{U}}} (1-x)^{C_{\bar{U}}} (1 + D_{\bar{U}} x), \\
x \bar{D}(x, \mu_{F,0}^2) &= A_{\bar{D}} x^{B_{\bar{D}}} (1-x)^{C_{\bar{D}}}.
\end{aligned} \tag{8}$$

Uncertainties in the fitted PDFs are determined using a similar procedure as the one described in Ref. [63]. Separate contributions for *fit*, *model*, *scale*, and *parametrization* uncertainties are obtained as described in the following.

The fit uncertainty represents the propagation to the PDFs of the uncertainties in the input measurements, theoretical predictions, and theory correction factors. It is estimated following the MC method outlined in Refs. [74, 75], whereby a large number of alternative fits (MC replicas) are performed with random variations of the input data according to their statistical and systematic uncertainties, taking the standard deviation of the resulting PDFs as an estimate of the fit uncertainty.

An alternative estimate for the fit uncertainty is obtained via the Hessian method [76] and found to be comparable to the MC fit uncertainty in most cases, apart from the u_v distribution, where it is found that the fit uncertainty is significantly underestimated by the Hessian method at $x < 0.1$. This is understood to be a consequence of the more flexible parametrization of u_v resulting from the parametrization scan, which is driven by the high- x region where the input data are constraining.

The model uncertainty arises from the choices made for the values of certain non-PDF parameters: the minimum Q^2 value used for restricting the HERA data, the strangeness fraction f_s , the charm and bottom quark masses m_c and m_b , and the value of the starting scale $\mu_{F,0}$. It is estimated by varying the values of these parameters up and down from their nominal values as indicated in Table 2, and adding the differences to the nominal fit result in quadrature separately for each variation direction.

Table 2: Nominal values and variations of parameters used to determine the PDF model uncertainty. Variations marked with an asterisk are in conflict with the requirement $\mu_{F,0} < m_c$ and thus cannot be used directly for the uncertainty estimation. Following Ref. [63], the results obtained for the opposite variation are symmetrized in these cases.

Parameter	Nominal value	Variations	
		down	up
Q_{\min}^2 (GeV ²)	10	7.5	12.5
f_s	0.4	0.3	0.5
m_c (GeV)	1.43	1.37*	1.49
m_b (GeV)	4.5	4.25	4.75
$\mu_{F,0}^2$ (GeV ²)	1.9	1.6	2.2*

A further uncertainty arises because of the choice of PDF parametrization. It is estimated by performing alternative fits that include one additional D or E parameter compared to the nominal parametrization. The maximum deviation between the nominal PDF and those obtained from the alternative parametrizations is taken as an additional parametrization uncertainty.

Finally, a scale uncertainty is estimated to account for missing higher orders in perturbation theory by varying μ_R and μ_F as described in Section 8. The envelope of the PDFs obtained with these alternative scale choices is defined as the scale uncertainty.

As discussed in Section 9, the level of agreement between the data and the theoretical predictions obtained with various global PDF sets varies according to the phase space region and is generally worse at outer rapidities. For the PDF determinations performed using the present data, a poor fit quality is observed in a small number of rapidity regions at high $|y|_{\max}$, y^* or y_b , with the partial χ^2 divided by the number of data points reaching values of ≈ 3 .

The effect of including these regions in the PDF determinations is investigated by comparing to fits performed with only a subset of rapidity regions, in which the data are well described by the theoretical predictions. While this results in an increased fit uncertainty, a sizable reduction in the parametrization uncertainty—and to a lesser extent the scale uncertainty—is achieved for the restricted fits. Consequently, the fit results are derived with the chosen subset of rapidity regions, which are indicated in Table 3 along with the total and partial χ^2 values, which are close to unity in most rapidity regions, except for the bin $0.5 < y_b < 1$, $y^* < 0.5$. The results of fits including all rapidity regions are provided for reference in Appendix A.

The PDFs resulting from the fits including the CMS dijet measurements are shown in Fig. 11, along with the different uncertainty contributions. The PDFs obtained with the inclusion of the 2D data are compatible with those obtained from the 3D data within the total uncertainty, which is obtained by adding together the parametrization uncertainty and the sum in quadrature of the fit, model, and scale uncertainty contributions. For most of the distributions, a smaller fit uncertainty is obtained in the 3D fit compared to the 2D one, while the model uncertainty is of a similar size, and the scale and parametrization uncertainties are slightly larger for the 3D fit in certain x regions.

To evaluate the impact of the present measurements on the PDF determination, fits are performed using the HERA DIS data alone, using the same PDF parametrization as for the fits including the dijet measurements. Figure 12 shows a comparison between the PDFs obtained using only the HERA DIS data, and those obtained when fitting the CMS dijet data in addition, along with the respective fit uncertainties. The distributions obtained with and without the inclusion of the dijet measurements are observed to be compatible with each other, and a general reduction in the fit uncertainty is observed when the CMS data is included in the fit. In particular, the precision of the gluon PDF is improved for parton momentum fractions $x > 0.1$, where the uncertainty is reduced by up to a factor of ≈ 2 by the inclusion of the dijet measurements. The 3D data are observed to constrain the gluon PDF to higher values of x compared to the 2D data.

For the PDF determinations presented above, the value of $\alpha_S(m_Z)$ is extracted from the data by including it in the fits as a free parameter, thus ensuring a consistent treatment of correlations between $\alpha_S(m_Z)$ and the PDF parameters, in particular those of the gluon distribution. The value of $\alpha_S(m_Z)$ obtained in the fit to the 2D dijet cross sections is

$$\begin{aligned} \alpha_S(m_Z) &= 0.1179 \pm 0.0015 \text{ (fit)} \pm 0.0008 \text{ (scale)} \pm 0.0008 \text{ (model)} \pm 0.0001 \text{ (param.)} \\ &= 0.1179 \pm 0.0019 \text{ (total)}, \end{aligned} \quad (9)$$

where the central value (fit uncertainty) is obtained as the average (standard deviation) over the ensemble of MC replicas. The remaining uncertainties are determined analogously to the PDFs, and in particular the parametrization uncertainty contributes linearly to the total uncertainty while the remaining contributions are added in quadrature. For the 3D dijet measurement, the

Table 3: Goodness-of-fit values for the fits to the HERA DIS data alone, and together with the CMS dijet measurements, using the PDF parametrization given in Eq. 8. The table shows the partial χ^2 values divided by the number of data points for the HERA DIS datasets and each of the dijet rapidity regions. The total χ^2 value, divided by the number of degrees of freedom, is given at the bottom of the table.

Data set	Partial χ^2 / n_{data}		
	HERA DIS	HERA DIS + CMS 13 TeV dijets	
	2D	3D	
CMS dijet 2D			
$ y _{\text{max}} < 0.5$		18 / 22	
$0.5 < y _{\text{max}} < 1$		15 / 22	
$1 < y _{\text{max}} < 1.5$		16 / 23	
$1.5 < y _{\text{max}} < 2$		15 / 12	
CMS dijet 3D			
$y_b < 0.5, \quad y^* < 0.5$		22 / 21	
$y_b < 0.5, \quad 0.5 < y^* < 1$		24 / 19	
$0.5 < y_b < 1, \quad y^* < 0.5$		49 / 19	
$0.5 < y_b < 1, \quad 0.5 < y^* < 1$		13 / 17	
$0.5 < y_b < 1, \quad 1 < y^* < 1.5$		8 / 7	
$1 < y_b < 1.5, \quad 0.5 < y^* < 1$		10 / 7	
$0.5 < y_b < 1, \quad 1.5 < y^* < 2$		9 / 6	
$1 < y_b < 1.5, \quad 1 < y^* < 1.5$		4 / 6	
$1.5 < y_b < 2, \quad 0.5 < y^* < 1$		8 / 5	
HERA1+2			
CC $e^-p, E_p = 920 \text{ GeV}$	51 / 42	51 / 42	50 / 42
CC $e^+p, E_p = 920 \text{ GeV}$	37 / 39	37 / 39	38 / 39
NC $e^-p, E_p = 920 \text{ GeV}$	221 / 159	222 / 159	221 / 159
NC $e^+p, E_p = 460 \text{ GeV}$	198 / 177	197 / 177	198 / 177
NC $e^+p, E_p = 575 \text{ GeV}$	186 / 221	186 / 221	186 / 221
NC $e^+p, E_p = 820 \text{ GeV}$	55 / 61	55 / 61	55 / 61
NC $e^+p, E_p = 920 \text{ GeV}$	359 / 317	364 / 317	362 / 317
Total χ^2 / n_{dof}	1161 / 1003	1232 / 1081	1339 / 1109

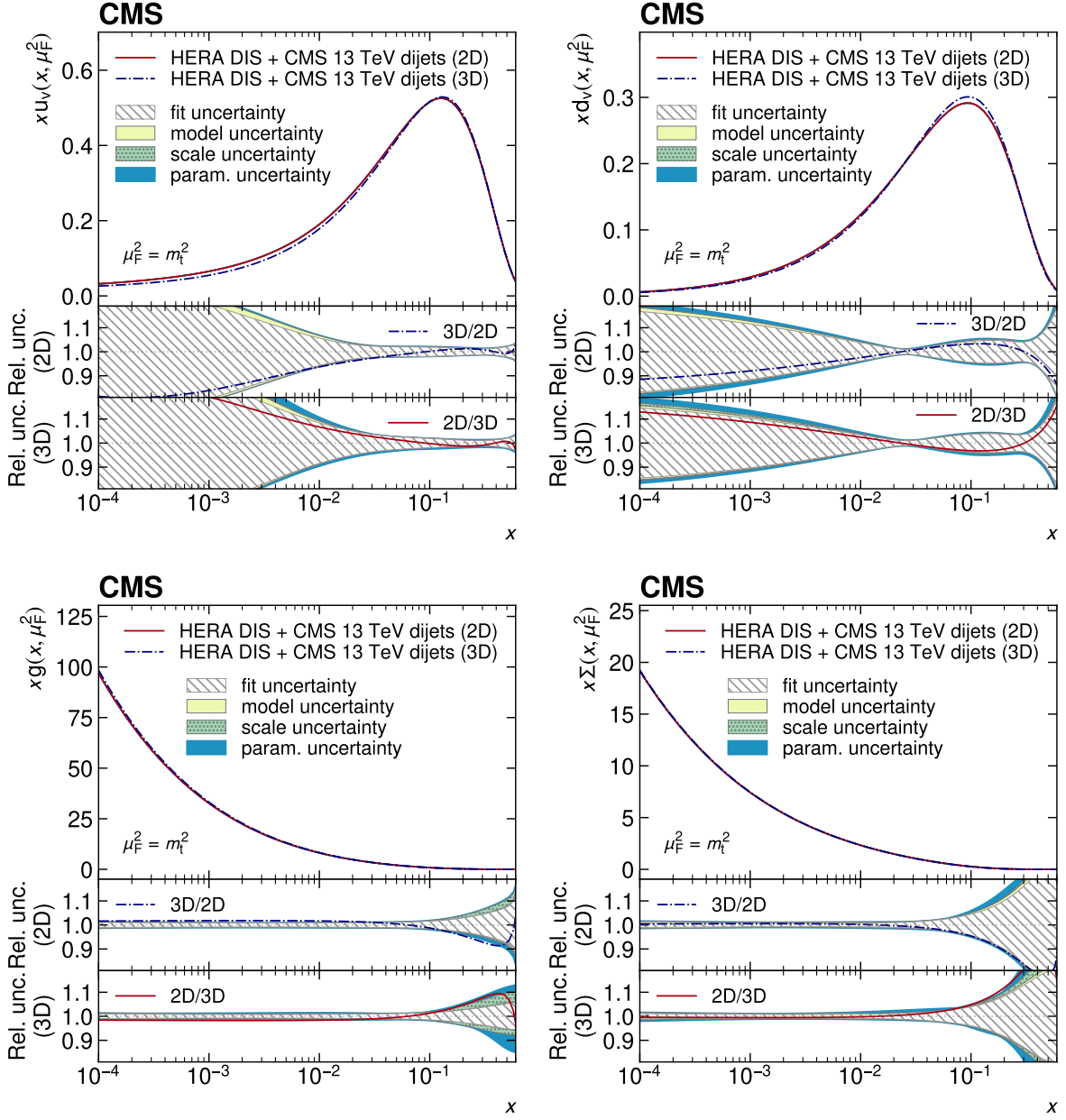


Figure 11: Parton distributions obtained in a fit to HERA DIS data together with the CMS 2D or 3D dijet measurements. The top panels show the PDFs of the up and down valence quarks (upper row), of the gluon (lower left), and of the total sea quarks (lower right) as a function of the fractional parton momentum x at a factorization scale equal to the top quark mass. The middle (lower) panels show the relative uncertainty contributions obtained for the 2D (3D) fit, as well as the ratios of the fitted central values.

result obtained is

$$\begin{aligned} \alpha_S(m_Z) &= 0.1181 \pm 0.0013 \text{ (fit)} \pm 0.0009 \text{ (scale)} \pm 0.0006 \text{ (model)} \pm 0.0002 \text{ (param.)} \\ &= 0.1181 \pm 0.0022 \text{ (total)}, \end{aligned} \quad (10)$$

which is in good agreement with the 2D result.

The values of $\alpha_S(m_Z)$ determined from the dijet measurements are in agreement with the

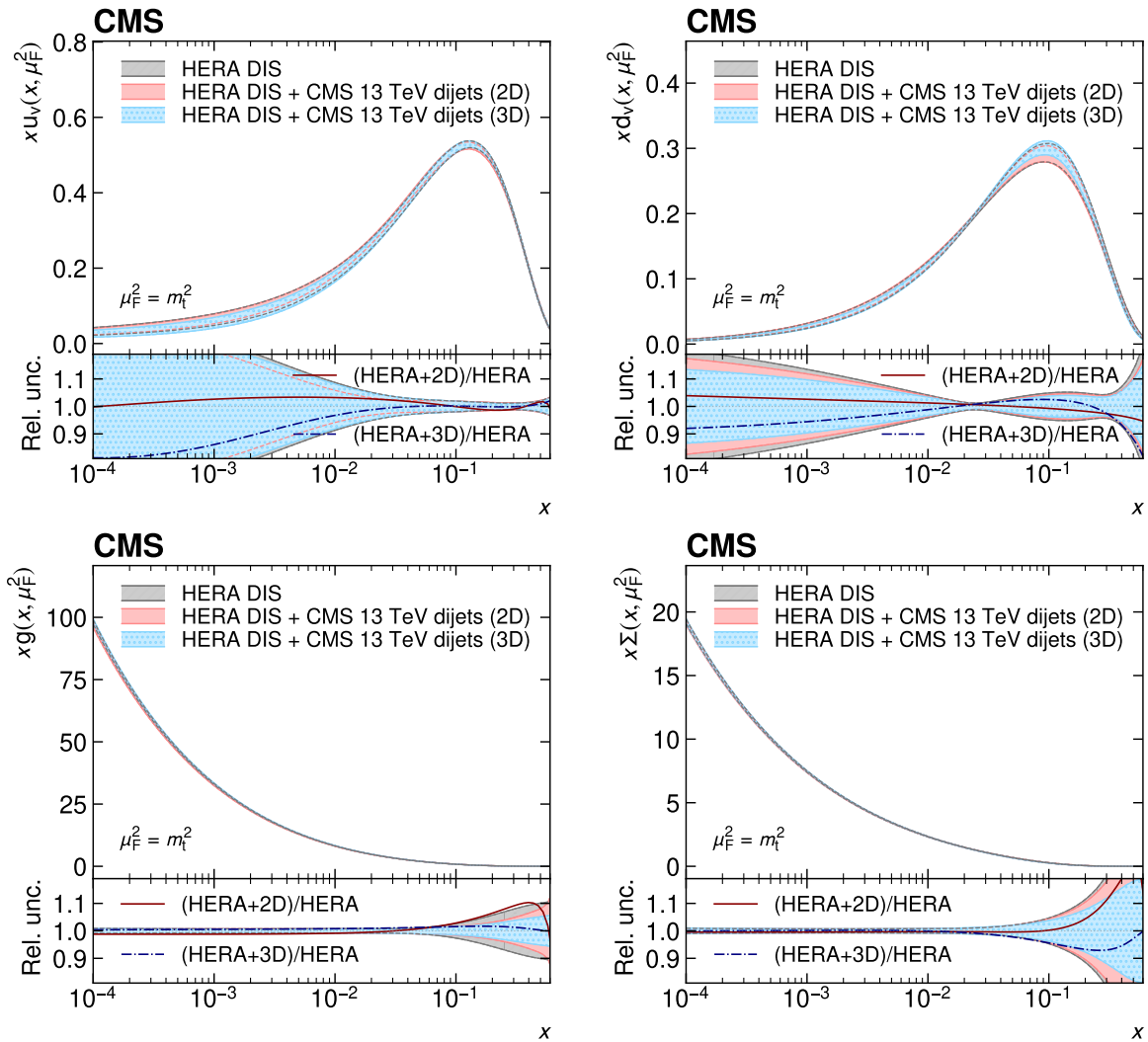


Figure 12: Parton distributions obtained in a fit to HERA DIS data together with the CMS dijet data, compared to a fit to HERA DIS data alone. Shown are the PDFs of the up and down valence quarks (upper row), of the gluon (lower left), and of the total sea quarks (lower right) as a function of the fractional parton momentum x at a factorization scale equal to the top quark mass. The bands indicate the fit uncertainty and are shown in the lower panels as a relative uncertainty with respect to the corresponding central values. The lines in the lower panels show the ratios between the fitted central values.

value of 0.1166 ± 0.0017 obtained in Ref. [62], and with the world average value of 0.1179 ± 0.0009 [77].

Parton distributions obtained in previous analyses at $\sqrt{s} = 8$ or 13 TeV of the inclusive jet [61, 62, 78] or the 3D dijet cross section [5] are not easily comparable directly because of significant differences in the fit setup, the PDF parametrizations, the model parameters, and particularly in the theoretical calculations at 8 TeV, which were only available at NLO. Taking the fit uncertainty in $\alpha_s(m_Z)$ obtained in a simultaneous fit with the PDFs as a figure of merit, the 13 TeV results are more precise, which is consistent with the increase in integrated luminosity.

11 Summary

The dijet production cross section is measured based on pp collision data recorded by the CMS detector in 2016 at $\sqrt{s} = 13$ TeV, corresponding to an integrated luminosity of up to 36.3 fb^{-1} .

The measurements are performed double-differentially (2D) as a function of the dijet invariant mass $m_{1,2}$ in five regions of the maximal absolute rapidity $|y|_{\text{max}}$ of the two jets with the largest transverse momenta, and triple-differentially (3D) as a function of either $m_{1,2}$ or the average transverse momentum $\langle p_T \rangle_{1,2}$ in 15 bins of the rapidity variables y^* and y_b . The latter two variables correspond to the rapidity separation of the two jets, and the total boost of the dijet system, respectively. All measurements are performed for jets clustered using the anti- k_T jet algorithm with distance parameters $R = 0.4$ and 0.8 , and the cross sections are unfolded in all measurement dimensions simultaneously to correct for detector effects.

This is the first time that such a large set of multidifferential dijet measurements for two observables, $\langle p_T \rangle_{1,2}$ and $m_{1,2}$, and two jet distance parameters, $R = 0.4$ and 0.8 , is made available for comparison to theory and use in fits of the parton distribution functions (PDFs) of the proton. Predictions at next-to-next-to-leading order (NNLO) in perturbative quantum chromodynamics, supplemented with electroweak and nonperturbative corrections are observed to describe the data better for $R = 0.8$.

Using the measurement of $m_{1,2}$ for $R = 0.8$, the PDFs of the proton are determined simultaneously in fits to the dijet measurements together with deep-inelastic scattering data from the HERA experiments following the approach described in earlier HERAPDF analyses [1, 2, 63]. The results obtained from the double- and triple-differential measurements are compatible within the estimated uncertainties. The inclusion of either of the dijet measurements leads to an improved determination of the PDFs compared to fits to HERA data alone. In particular, the uncertainty in the gluon distribution at fractional proton momenta $x > 0.1$ is reduced, with the 3D dijet data providing tighter constraints at higher values of x compared to the 2D data. The strong coupling constant at the Z boson mass is determined simultaneously with the PDFs, yielding consistent results between the 2D and 3D dijet measurements, with the former resulting in the slightly more precise value of $\alpha_S(m_Z) = 0.1179 \pm 0.0019$ at NNLO.

The impact of subleading-color contributions to the leading-color NNLO calculation used here is not yet known [42]. Apart from being useful as inputs to PDF fits or studies of jet size dependence, the present 2D and 3D measurements for two jet size parameters, $R = 0.4$ and 0.8 , and for the two dijet observables $m_{1,2}$ and $\langle p_T \rangle_{1,2}$, provide an ideal testing ground for further investigations.

Acknowledgments

We congratulate our colleagues in the CERN accelerator departments for the excellent performance of the LHC and thank the technical and administrative staffs at CERN and at other CMS institutes for their contributions to the success of the CMS effort. In addition, we gratefully acknowledge the computing centers and personnel of the Worldwide LHC Computing Grid and other centers for delivering so effectively the computing infrastructure essential to our analyses. Finally, we acknowledge the enduring support for the construction and operation of the LHC, the CMS detector, and the supporting computing infrastructure provided by the following funding agencies: SC (Armenia), BMBWF and FWF (Austria); FNRS and FWO (Belgium); CNPq, CAPES, FAPERJ, FAPERGS, and FAPESP (Brazil); MES and BNSF (Bulgaria); CERN; CAS, MoST, and NSFC (China); MINCIENCIAS (Colombia); MSES and CSF (Croatia);

RIF (Cyprus); SENESCYT (Ecuador); MoER, ERC PUT and ERDF (Estonia); Academy of Finland, MEC, and HIP (Finland); CEA and CNRS/IN2P3 (France); SRNSF (Georgia); BMBF, DFG, and HGF (Germany); GSRI (Greece); NKFIH (Hungary); DAE and DST (India); IPM (Iran); SFI (Ireland); INFN (Italy); MSIP and NRF (Republic of Korea); MES (Latvia); LAS (Lithuania); MOE and UM (Malaysia); BUAP, CINVESTAV, CONACYT, LNS, SEP, and UASLP-FAI (Mexico); MOS (Montenegro); MBIE (New Zealand); PAEC (Pakistan); MES and NSC (Poland); FCT (Portugal); MESTD (Serbia); MCIN/AEI and PCTI (Spain); MOSTR (Sri Lanka); Swiss Funding Agencies (Switzerland); MST (Taipei); MHESI and NSTDA (Thailand); TUBITAK and TEN-MAK (Turkey); NASU (Ukraine); STFC (United Kingdom); DOE and NSF (USA).

Individuals have received support from the Marie-Curie program and the European Research Council and Horizon 2020 Grant, contract Nos. 675440, 724704, 752730, 758316, 765710, 824093, and COST Action CA16108 (European Union); the Leventis Foundation; the Alfred P. Sloan Foundation; the Alexander von Humboldt Foundation; the Science Committee, project no. 22rl-037 (Armenia); the Belgian Federal Science Policy Office; the Fonds pour la Formation à la Recherche dans l'Industrie et dans l'Agriculture (FRIA-Belgium); the Agentschap voor Innovatie door Wetenschap en Technologie (IWT-Belgium); the F.R.S.-FNRS and FWO (Belgium) under the "Excellence of Science – EOS" – be.h project n. 30820817; the Beijing Municipal Science & Technology Commission, No. Z191100007219010 and Fundamental Research Funds for the Central Universities (China); the Ministry of Education, Youth and Sports (MEYS) of the Czech Republic; the Shota Rustaveli National Science Foundation, grant FR-22-985 (Georgia); the Deutsche Forschungsgemeinschaft (DFG), under Germany's Excellence Strategy – EXC 2121 "Quantum Universe" – 390833306, and under project number 400140256 - GRK2497; the Hellenic Foundation for Research and Innovation (HFRI), Project Number 2288 (Greece); the Hungarian Academy of Sciences, the New National Excellence Program - ÚNKP, the NKFIH research grants K 124845, K 124850, K 128713, K 128786, K 129058, K 131991, K 133046, K 138136, K 143460, K 143477, 2020-2.2.1-ED-2021-00181, and TKP2021-NKTA-64 (Hungary); the Council of Science and Industrial Research, India; ICSC – National Research Center for High Performance Computing, Big Data and Quantum Computing, funded by the EU NexGeneration program (Italy); the Latvian Council of Science; the Ministry of Education and Science, project no. 2022/WK/14, and the National Science Center, contracts Opus 2021/41/B/ST2/01369 and 2021/43/B/ST2/01552 (Poland); the Fundação para a Ciência e a Tecnologia, grant CEECIND/01334/2018 (Portugal); the National Priorities Research Program by Qatar National Research Fund; MCIN/AEI/10.13039/501100011033, ERDF "a way of making Europe", and the Programa Estatal de Fomento de la Investigación Científica y Técnica de Excelencia María de Maeztu, grant MDM-2017-0765 and Programa Severo Ochoa del Principado de Asturias (Spain); the Chulalongkorn Academic into Its 2nd Century Project Advancement Project, and the National Science, Research and Innovation Fund via the Program Management Unit for Human Resources & Institutional Development, Research and Innovation, grant B37G660013 (Thailand); the Kavli Foundation; the Nvidia Corporation; the SuperMicro Corporation; the Welch Foundation, contract C-1845; and the Weston Havens Foundation (USA).

References

- [1] H1 and ZEUS Collaborations, "Combined measurement and QCD analysis of the inclusive $e^\pm p$ scattering cross sections at HERA", *JHEP* **01** (2010) 109, doi:10.1007/JHEP01(2010)109, arXiv:0911.0884.
- [2] H1 and ZEUS Collaborations, "Combination of measurements of inclusive deep inelastic

- $e^\pm p$ scattering cross sections and QCD analysis of HERA data”, *Eur. Phys. J. C* **75** (2015) 580, doi:10.1140/epjc/s10052-015-3710-4, arXiv:1506.06042.
- [3] J. Currie et al., “Precise predictions for dijet production at the LHC”, *Phys. Rev. Lett.* **119** (2017) 152001, doi:10.1103/PhysRevLett.119.152001, arXiv:1705.10271.
- [4] A. Gehrmann-De Ridder et al., “Triple differential dijet cross section at the LHC”, *Phys. Rev. Lett.* **123** (2019) 102001, doi:10.1103/PhysRevLett.123.102001, arXiv:1905.09047.
- [5] CMS Collaboration, “Measurement of the triple-differential dijet cross section in proton-proton collisions at $\sqrt{s} = 8$ TeV and constraints on parton distribution functions”, *Eur. Phys. J. C* **77** (2017) 746, doi:10.1140/epjc/s10052-017-5286-7, arXiv:1705.02628.
- [6] M. Cacciari, G. P. Salam, and G. Soyez, “The anti- k_T jet clustering algorithm”, *JHEP* **04** (2008) 063, doi:10.1088/1126-6708/2008/04/063, arXiv:0802.1189.
- [7] M. Cacciari, G. P. Salam, and G. Soyez, “FastJet user manual”, *Eur. Phys. J. C* **72** (2012) 1896, doi:10.1140/epjc/s10052-012-1896-2, arXiv:1111.6097.
- [8] ATLAS Collaboration, “Measurement of inclusive jet and dijet cross sections in proton-proton collisions at 7 TeV centre-of-mass energy with the ATLAS detector”, *Eur. Phys. J. C* **71** (2011) 1512, doi:10.1140/epjc/s10052-010-1512-2, arXiv:1009.5908.
- [9] CMS Collaboration, “Measurement of the differential dijet production cross section in proton-proton collisions at $\sqrt{s} = 7$ TeV”, *Phys. Lett. B* **700** (2011) 187, doi:10.1016/j.physletb.2011.05.027, arXiv:1104.1693.
- [10] CMS Collaboration, “Measurements of differential jet cross sections in proton-proton collisions at $\sqrt{s} = 7$ TeV with the CMS detector”, *Phys. Rev. D* **87** (2013) 112002, doi:10.1103/PhysRevD.87.112002, arXiv:1212.6660. [Erratum: doi:10.1103/PhysRevD.87.119902].
- [11] ATLAS Collaboration, “Measurement of dijet cross sections in pp collisions at 7 TeV centre-of-mass energy using the ATLAS detector”, *JHEP* **05** (2014) 059, doi:10.1007/JHEP05(2014)059, arXiv:1312.3524.
- [12] ATLAS Collaboration, “Measurement of inclusive jet and dijet cross-sections in proton-proton collisions at $\sqrt{s} = 13$ TeV with the ATLAS detector”, *JHEP* **05** (2018) 195, doi:10.1007/JHEP05(2018)195, arXiv:1711.02692.
- [13] HEPData record for this analysis, 2023. doi:10.17182/hepdata.NNNNN.
- [14] CMS Collaboration, “The CMS trigger system”, *JINST* **12** (2017) P01020, doi:10.1088/1748-0221/12/01/P01020, arXiv:1609.02366.
- [15] CMS Collaboration, “Performance of the CMS Level-1 trigger in proton-proton collisions at $\sqrt{s} = 13$ TeV”, *JINST* **15** (2020) P10017, doi:10.1088/1748-0221/15/10/P10017, arXiv:2006.10165.
- [16] CMS Collaboration, “The CMS experiment at the CERN LHC”, *JINST* **3** (2008) S08004, doi:10.1088/1748-0221/3/08/S08004.

- [17] T. Sjöstrand et al., “An introduction to PYTHIA 8.2”, *Comput. Phys. Commun.* **191** (2015) 159, doi:10.1016/j.cpc.2015.01.024, arXiv:1410.3012.
- [18] CMS Collaboration, “Event generator tunes obtained from underlying event and multiparton scattering measurements”, *Eur. Phys. J. C* **76** (2016) 155, doi:10.1140/epjc/s10052-016-3988-x, arXiv:1512.00815.
- [19] J. Alwall et al., “The automated computation of tree-level and next-to-leading order differential cross sections, and their matching to parton shower simulations”, *JHEP* **07** (2014) 079, doi:10.1007/JHEP07(2014)079, arXiv:1405.0301.
- [20] GEANT4 Collaboration, “GEANT4—a simulation toolkit”, *Nucl. Instrum. Meth. A* **506** (2003) 250, doi:10.1016/S0168-9002(03)01368-8.
- [21] CMS Collaboration, “Measurement of the inelastic proton-proton cross section at $\sqrt{s} = 13$ TeV”, *JHEP* **07** (2018) 161, doi:10.1007/JHEP07(2018)161, arXiv:1802.02613.
- [22] CMS Collaboration, “Pileup mitigation at CMS in 13 TeV data”, *JINST* **15** (2020) P09018, doi:10.1088/1748-0221/15/09/P09018, arXiv:2003.00503.
- [23] CMS Collaboration, “Particle-flow reconstruction and global event description with the CMS detector”, *JINST* **12** (2017) P10003, doi:10.1088/1748-0221/12/10/P10003, arXiv:1706.04965.
- [24] CMS Collaboration, “Technical proposal for the Phase-II upgrade of the Compact Muon Solenoid”, CMS Technical Proposal CERN-LHCC-2015-010, CMS-TDR-15-02, 2015.
- [25] CMS Collaboration, “Study of pileup removal algorithms for jets”, CMS Physics Analysis Summary CMS-PAS-JME-14-001, 2014.
- [26] CMS Collaboration, “Jet energy scale and resolution in the CMS experiment in pp collisions at 8 TeV”, *JINST* **12** (2017) P02014, doi:10.1088/1748-0221/12/02/P02014, arXiv:1607.03663.
- [27] CMS Collaboration, “Jet algorithms performance in 13 TeV data”, CMS Physics Analysis Summary CMS-PAS-JME-16-003, 2017.
- [28] CMS Collaboration, “Performance of missing transverse momentum reconstruction in proton-proton collisions at $\sqrt{s} = 13$ TeV using the CMS detector”, *JINST* **14** (2019) P07004, doi:10.1088/1748-0221/14/07/P07004, arXiv:1903.06078.
- [29] S. Schmitt, “TUnfold: an algorithm for correcting migration effects in high energy physics”, *JINST* **7** (2012) T10003, doi:10.1088/1748-0221/7/10/T10003, arXiv:1205.6201.
- [30] CMS Collaboration, “Jet energy scale and resolution performance with 13 TeV data collected by CMS in 2016–2018”, CMS Detector Performance Note CMS-DP-2020-019, 2020.
- [31] CMS Collaboration, “Precision luminosity measurement in proton-proton collisions at $\sqrt{s} = 13$ TeV in 2015 and 2016 at CMS”, *Eur. Phys. J. C* **81** (2021) 800, doi:10.1140/epjc/s10052-021-09538-2, arXiv:2104.01927.

- [32] T. Gehrmann et al., “Jet cross sections and transverse momentum distributions with NNLOJET”, in *Proceedings of 13th International Symposium on Radiative Corrections (Applications of Quantum Field Theory to Phenomenology) — PoS(RADCOR2017)*, volume 290, p. 074. 2018. arXiv:1801.06415. doi:10.22323/1.290.0074.
- [33] T. Kluge, K. Rabbertz, and M. Wobisch, “fastNLO: Fast pQCD calculations for PDF fits”, in *Proc. 14th Intern. Workshop on Deep-Inelastic Scattering (DIS 2006)*, p. 483. Tsukuba, Japan, 20-24 April, 2006. arXiv:hep-ph/0609285. doi:10.1142/9789812706706_0110.
- [34] D. Britzger, K. Rabbertz, F. Stober, and M. Wobisch, “New features in version 2 of the fastNLO project”, in *Proc. 20th Intern. Workshop on Deep-Inelastic Scattering and Related Subjects*, p. 217. 2012. arXiv:1208.3641. doi:10.3204/DESY-PROC-2012-02/165.
- [35] D. Britzger et al., “Calculations for deep inelastic scattering using fast interpolation grid techniques at NNLO in QCD and the extraction of α_s from HERA data”, *Eur. Phys. J. C* **79** (2019) 845, doi:10.1140/epjc/s10052-019-7351-x, arXiv:1906.05303.
- [36] D. Britzger et al., “NNLO interpolation grids for jet production at the LHC”, *Eur. Phys. J. C* **82** (2022) 930, doi:10.1140/epjc/s10052-022-10880-2, arXiv:2207.13735.
- [37] J. Currie et al., “Jet cross sections at the LHC with NNLOJET”, in *Proceedings of Loops and Legs in Quantum Field Theory — PoS(LL2018)*, volume 303, p. 001. 2018. arXiv:1807.06057. doi:10.22323/1.303.0001.
- [38] M. Cacciari et al., “The $t\bar{t}$ cross-section at 1.8 TeV and 1.96 TeV: a study of the systematics due to parton densities and scale dependence”, *JHEP* **04** (2004) 068, doi:10.1088/1126-6708/2004/04/068, arXiv:hep-ph/0303085.
- [39] S. Catani, D. de Florian, M. Grazzini, and P. Nason, “Soft-gluon resummation for Higgs boson production at hadron colliders”, *JHEP* **07** (2003) 028, doi:10.1088/1126-6708/2003/07/028, arXiv:hep-ph/0306211.
- [40] A. Banfi, G. P. Salam, and G. Zanderighi, “Phenomenology of event shapes at hadron colliders”, *JHEP* **06** (2010) 038, doi:10.1007/JHEP06(2010)038, arXiv:1001.4082.
- [41] J. Currie, E. W. N. Glover, and J. Pires, “Next-to-next-to leading order QCD predictions for single jet inclusive production at the LHC”, *Phys. Rev. Lett.* **118** (2017) 072002, doi:10.1103/PhysRevLett.118.072002, arXiv:1611.01460.
- [42] X. Chen et al., “NNLO QCD corrections in full colour for jet production observables at the LHC”, *JHEP* **09** (2022) 025, doi:10.1007/JHEP09(2022)025, arXiv:2204.10173.
- [43] CMS Collaboration, “Measurement of the double-differential inclusive jet cross section in proton-proton collisions at $\sqrt{s} = 13$ TeV”, *Eur. Phys. J. C* **76** (2016) 451, doi:10.1140/epjc/s10052-016-4286-3, arXiv:1605.04436.
- [44] CMS Collaboration, “Investigations of the impact of the parton shower tuning in PYTHIA 8 in the modelling of $t\bar{t}$ at $\sqrt{s} = 8$ and 13 TeV”, CMS Physics Analysis Summary CMS-PAS-TOP-16-021, 2016.
- [45] M. Bähr et al., “HERWIG++ physics and manual”, *Eur. Phys. J. C* **58** (2008) 639, doi:10.1140/epjc/s10052-008-0798-9, arXiv:0803.0883.

- [46] M. H. Seymour and A. Siódmok, “Constraining MPI models using σ_{eff} and recent Tevatron and LHC underlying event data”, *JHEP* **10** (2013) 113, doi:10.1007/JHEP10(2013)113, arXiv:1307.5015.
- [47] P. Nason, “A new method for combining NLO QCD with shower Monte Carlo algorithms”, *JHEP* **11** (2004) 040, doi:10.1088/1126-6708/2004/11/040, arXiv:hep-ph/0409146.
- [48] S. Frixione, P. Nason, and C. Oleari, “Matching NLO QCD computations with parton shower simulations: the POWHEG method”, *JHEP* **11** (2007) 070, doi:10.1088/1126-6708/2007/11/070, arXiv:0709.2092.
- [49] S. Alioli, P. Nason, C. Oleari, and E. Re, “A general framework for implementing NLO calculations in shower Monte Carlo programs: the POWHEG BOX”, *JHEP* **06** (2010) 043, doi:10.1007/JHEP06(2010)043, arXiv:1002.2581.
- [50] S. Alioli et al., “Jet pair production in POWHEG”, *JHEP* **04** (2011) 081, doi:10.1007/JHEP04(2011)081, arXiv:1012.3380.
- [51] J. Bellm et al., “HERWIG 7.0/HERWIG++ 3.0 release note”, *Eur. Phys. J. C* **76** (2016) 196, doi:10.1140/epjc/s10052-016-4018-8, arXiv:1512.01178.
- [52] CMS Collaboration, “Development and validation of HERWIG 7 tunes from CMS underlying-event measurements”, *Eur. Phys. J. C* **81** (2021) 312, doi:10.1140/epjc/s10052-021-08949-5, arXiv:2011.03422.
- [53] S. Dittmaier, A. Huss, and C. Speckner, “Weak radiative corrections to dijet production at hadron colliders”, *JHEP* **11** (2012) 095, doi:10.1007/JHEP11(2012)095, arXiv:1210.0438.
- [54] A. Buckley et al., “LHAPDF6: parton density access in the LHC precision era”, *Eur. Phys. J. C* **75** (2015) 132, doi:10.1140/epjc/s10052-015-3318-8, arXiv:1412.7420.
- [55] S. Alekhin, J. Blümlein, S. Moch, and R. Plačakytė, “Parton distribution functions, α_s , and heavy-quark masses for LHC Run II”, *Phys. Rev. D* **96** (2017) 014011, doi:10.1103/PhysRevD.96.014011, arXiv:1701.05838.
- [56] T.-J. Hou et al., “New CTEQ global analysis of quantum chromodynamics with high-precision data from the LHC”, *Phys. Rev. D* **103** (2021) 014013, doi:10.1103/PhysRevD.103.014013, arXiv:1912.10053.
- [57] S. Bailey et al., “Parton distributions from LHC, HERA, Tevatron and fixed target data: MSHT20 PDFs”, *Eur. Phys. J. C* **81** (2021) 341, doi:10.1140/epjc/s10052-021-09057-0, arXiv:2012.04684.
- [58] NNPDF Collaboration, “Parton distributions from high-precision collider data”, *Eur. Phys. J. C* **77** (2017) 663, doi:10.1140/epjc/s10052-017-5199-5, arXiv:1706.00428.
- [59] CMS Collaboration, “Measurement of the ratio of inclusive jet cross sections using the anti- k_T algorithm with radius parameters $R = 0.5$ and 0.7 in pp collisions at $\sqrt{s} = 7$ TeV”, *Phys. Rev. D* **90** (2014) 072006, doi:10.1103/PhysRevD.90.072006, arXiv:1406.0324.

-
- [60] ATLAS Collaboration, “Measurement of the inclusive jet cross-sections in proton–proton collisions at $\sqrt{s} = 8$ TeV with the ATLAS detector”, *JHEP* **09** (2017) 020, doi:10.1007/JHEP09(2017)020, arXiv:1706.03192.
- [61] CMS Collaboration, “Measurement and QCD analysis of double-differential inclusive jet cross sections in proton-proton collisions at $\sqrt{s} = 13$ TeV”, *JHEP* **02** (2022) 142, doi:10.1007/JHEP02(2022)142, arXiv:2111.10431.
- [62] CMS Collaboration, “Addendum to: Measurement and QCD analysis of double-differential inclusive jet cross sections in proton-proton collisions at $\sqrt{s} = 13$ TeV”, *JHEP* **12** (2022) 035, doi:10.1007/JHEP12(2022)035, arXiv:2111.10431.
- [63] H1 and ZEUS Collaborations, “Impact of jet-production data on the next-to-next-to-leading-order determination of HERAPDF2.0 parton distributions”, *Eur. Phys. J. C* **82** (2022) 243, doi:10.1140/epjc/s10052-022-10083-9, arXiv:2112.01120.
- [64] J. Bellm et al., “Jet cross sections at the LHC and the quest for higher precision”, *Eur. Phys. J. C* **80** (2020) 93, doi:10.1140/epjc/s10052-019-7574-x, arXiv:1903.12563.
- [65] S. Alekhin et al., “HERAFitter: open source QCD fit project”, *Eur. Phys. J. C* **75** (2015) 304, doi:10.1140/epjc/s10052-015-3480-z, arXiv:1410.4412.
- [66] V. Bertone et al., “xFitter 2.0.0: An open source QCD fit framework”, in *Proceedings of XXV International Workshop on Deep-Inelastic Scattering and Related Subjects — PoS(DIS2017)*, volume 297, p. 203. 2017. arXiv:1709.01151. doi:10.22323/1.297.0203.
- [67] Y. L. Dokshitzer, “Calculation of the structure functions for deep inelastic scattering and e^+e^- annihilation by perturbation theory in quantum chromodynamics”, *Sov. Phys. JETP* **46** (1977) 641.
- [68] V. N. Gribov and L. N. Lipatov, “Deep inelastic ep scattering in perturbation theory”, *Sov. J. Nucl. Phys.* **15** (1972) 438.
- [69] G. Altarelli and G. Parisi, “Asymptotic freedom in parton language”, *Nucl. Phys. B* **126** (1977) 298, doi:10.1016/0550-3213(77)90384-4.
- [70] M. Botje, “QCDNUM: Fast QCD evolution and convolution”, *Comput. Phys. Commun.* **182** (2011) 490, doi:10.1016/j.cpc.2010.10.020, arXiv:1005.1481.
- [71] R. S. Thorne and R. G. Roberts, “Ordered analysis of heavy flavor production in deep inelastic scattering”, *Phys. Rev. D* **57** (1998) 6871, doi:10.1103/PhysRevD.57.6871, arXiv:hep-ph/9709442.
- [72] R. S. Thorne, “Variable-flavor number scheme for next-to-next-to-leading order”, *Phys. Rev. D* **73** (2006) 054019, doi:10.1103/PhysRevD.73.054019, arXiv:hep-ph/0601245.
- [73] R. S. Thorne, “Effect of changes of variable flavor number scheme on parton distribution functions and predicted cross sections”, *Phys. Rev. D* **86** (2012) 074017, doi:10.1103/PhysRevD.86.074017, arXiv:1201.6180.

- [74] W. T. Giele and S. Keller, “Implications of hadron collider observables on parton distribution function uncertainties”, *Phys. Rev. D* **58** (1998) 094023, doi:10.1103/PhysRevD.58.094023, arXiv:hep-ph/9803393.
- [75] W. T. Giele, S. A. Keller, and D. A. Kosower, “Parton distribution function uncertainties”, 2001. arXiv:hep-ph/0104052.
- [76] J. Pumplin et al., “Uncertainties of predictions from parton distribution functions. II. The Hessian method”, *Phys. Rev. D* **65** (2001) 014013, doi:10.1103/PhysRevD.65.014013, arXiv:hep-ph/0101032.
- [77] Particle Data Group, R. L. Workman et al., “Review of particle physics”, *Prog. Theor. Exp. Phys.* **2022** (2022) 083C01, doi:10.1093/ptep/ptac097.
- [78] CMS Collaboration, “Measurement and QCD analysis of double-differential inclusive jet cross sections in pp collisions at $\sqrt{s} = 8$ TeV and cross section ratios to 2.76 and 7 TeV”, *JHEP* **03** (2017) 156, doi:10.1007/JHEP03(2017)156, arXiv:1609.05331.

A Full-rapidity fit results

This section documents the results obtained for the fits described in Section 10 when all dijet rapidity regions are included. The partial χ^2 values indicating the goodness-of-fit in each rapidity region are given in Table 4, and Eqs. (11) and (12) show the values of $\alpha_S(m_Z)$ obtained in fits including the 2D and 3D dijet cross sections, respectively:

$$\alpha_S(m_Z)_{2D} = 0.1201 \pm 0.0012 \text{ (fit)} \pm 0.0008 \text{ (scale)} \pm 0.0008 \text{ (model)} \pm 0.0005 \text{ (param.)}, \quad (11)$$

$$\alpha_S(m_Z)_{3D} = 0.1201 \pm 0.0010 \text{ (fit)} \pm 0.0005 \text{ (scale)} \pm 0.0008 \text{ (model)} \pm 0.0006 \text{ (param.)}. \quad (12)$$

Table 4: Goodness-of-fit values for the fits to the HERA DIS data alone, and together with the CMS dijet measurements, including all rapidity regions. The table shows the partial χ^2 values divided by the number of data points for the HERA DIS datasets and each of the dijet rapidity regions. The total χ^2 value, divided by the number of degrees of freedom, is given at the bottom of the table.

Data set	Partial χ^2 / n_{data}	
	HERA DIS + CMS 13 TeV dijets 2D	3D
CMS dijet 2D		
$ y _{\text{max}} < 0.5$	24 / 22	
$0.5 < y _{\text{max}} < 1$	14 / 22	
$1 < y _{\text{max}} < 1.5$	22 / 23	
$1.5 < y _{\text{max}} < 2$	15 / 12	
$2 < y _{\text{max}} < 2.5$	30 / 12	
CMS dijet 3D		
$y_b < 0.5, \quad y^* < 0.5$		32 / 21
$y_b < 0.5, \quad 0.5 < y^* < 1$		23 / 19
$0.5 < y_b < 1, \quad y^* < 0.5$		40 / 19
$y_b < 0.5, \quad 1 < y^* < 1.5$		45 / 17
$0.5 < y_b < 1, \quad 0.5 < y^* < 1$		18 / 17
$1 < y_b < 1.5, \quad y^* < 0.5$		44 / 17
$y_b < 0.5, \quad 1.5 < y^* < 2$		15 / 7
$0.5 < y_b < 1, \quad 1 < y^* < 1.5$		7 / 7
$1 < y_b < 1.5, \quad 0.5 < y^* < 1$		9 / 7
$1.5 < y_b < 2, \quad y^* < 0.5$		20 / 6
$y_b < 0.5, \quad 2 < y^* < 2.5$		19 / 6
$0.5 < y_b < 1, \quad 1.5 < y^* < 2$		16 / 6
$1 < y_b < 1.5, \quad 1 < y^* < 1.5$		6 / 6
$1.5 < y_b < 2, \quad 0.5 < y^* < 1$		1 / 5
$2 < y_b < 2.5, \quad y^* < 0.5$		15 / 4
HERA1+2		
CC $e^-p, E_p = 920 \text{ GeV}$	50 / 42	48 / 42
CC $e^+p, E_p = 920 \text{ GeV}$	37 / 39	41 / 39
NC $e^-p, E_p = 920 \text{ GeV}$	222 / 159	227 / 159
NC $e^+p, E_p = 460 \text{ GeV}$	197 / 177	201 / 177
NC $e^+p, E_p = 575 \text{ GeV}$	186 / 221	187 / 221
NC $e^+p, E_p = 820 \text{ GeV}$	55 / 61	55 / 61
NC $e^+p, E_p = 920 \text{ GeV}$	368 / 317	365 / 317
Total χ^2 / n_{dof}	1283 / 1094	1557 / 1167

B Additional figures

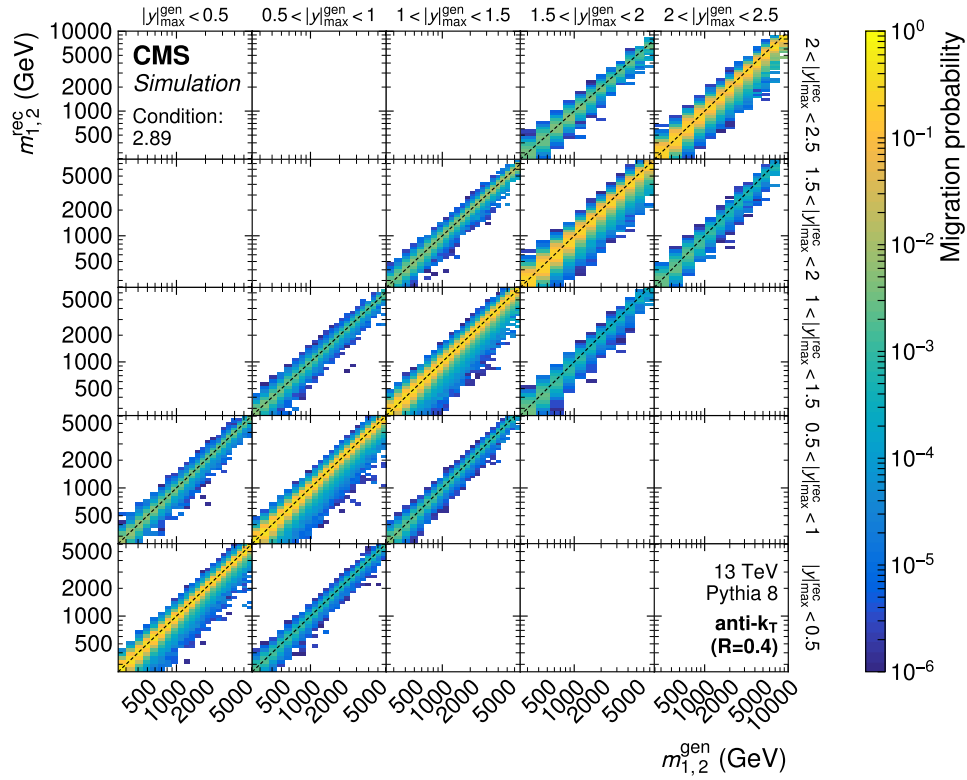


Figure 13: Response matrices for the 2D measurements as a function of $|y|_{\max}$ and $m_{1,2}$ for jets with $R = 0.4$. The details correspond to those of Fig. 2.

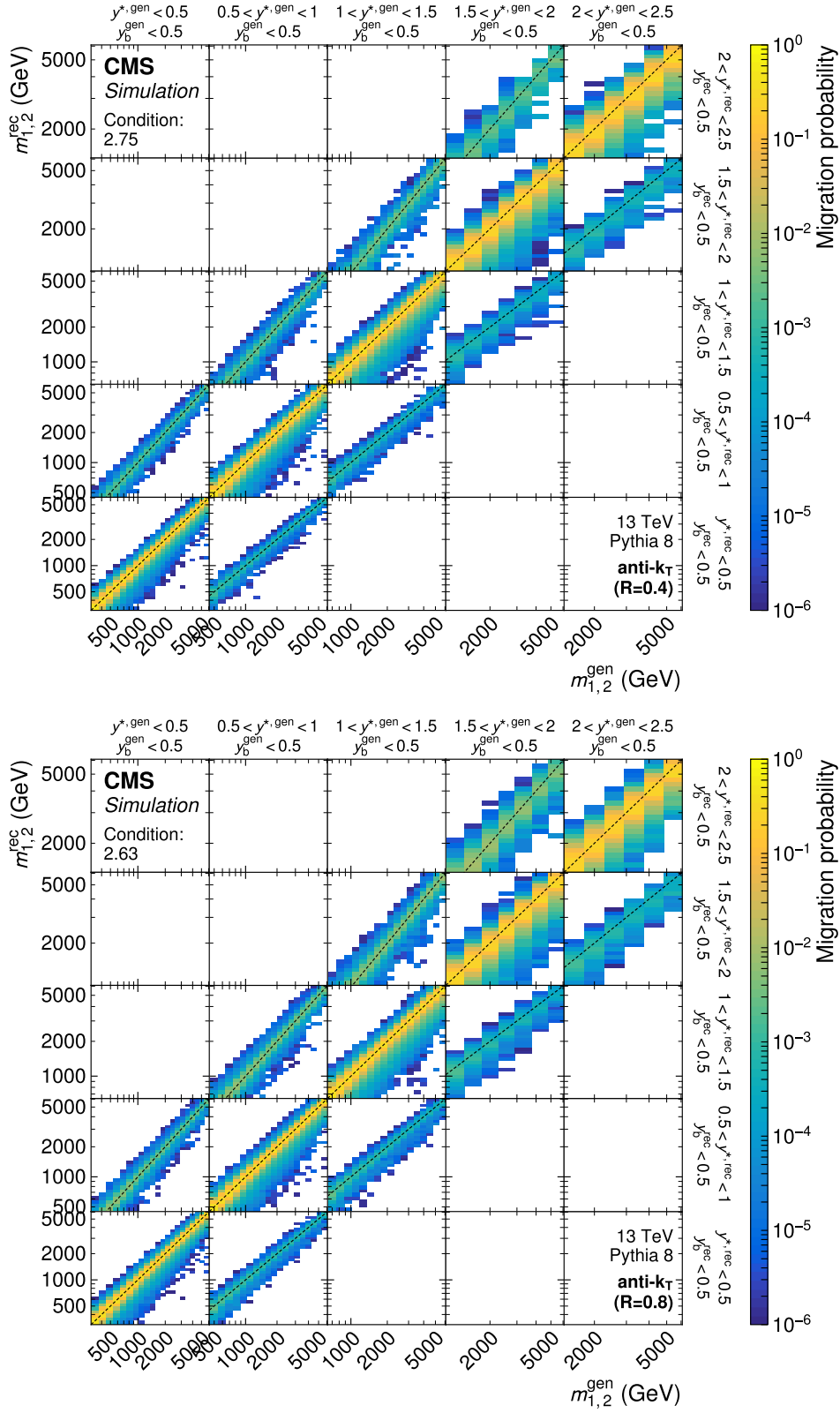


Figure 14: Partial response matrices for the 3D measurements as a function of $m_{1,2}$ using jets with $R = 0.4$ (upper) and 0.8 (lower), shown here for the five rapidity regions with $y_b < 0.5$. The details correspond to those of Fig. 2.

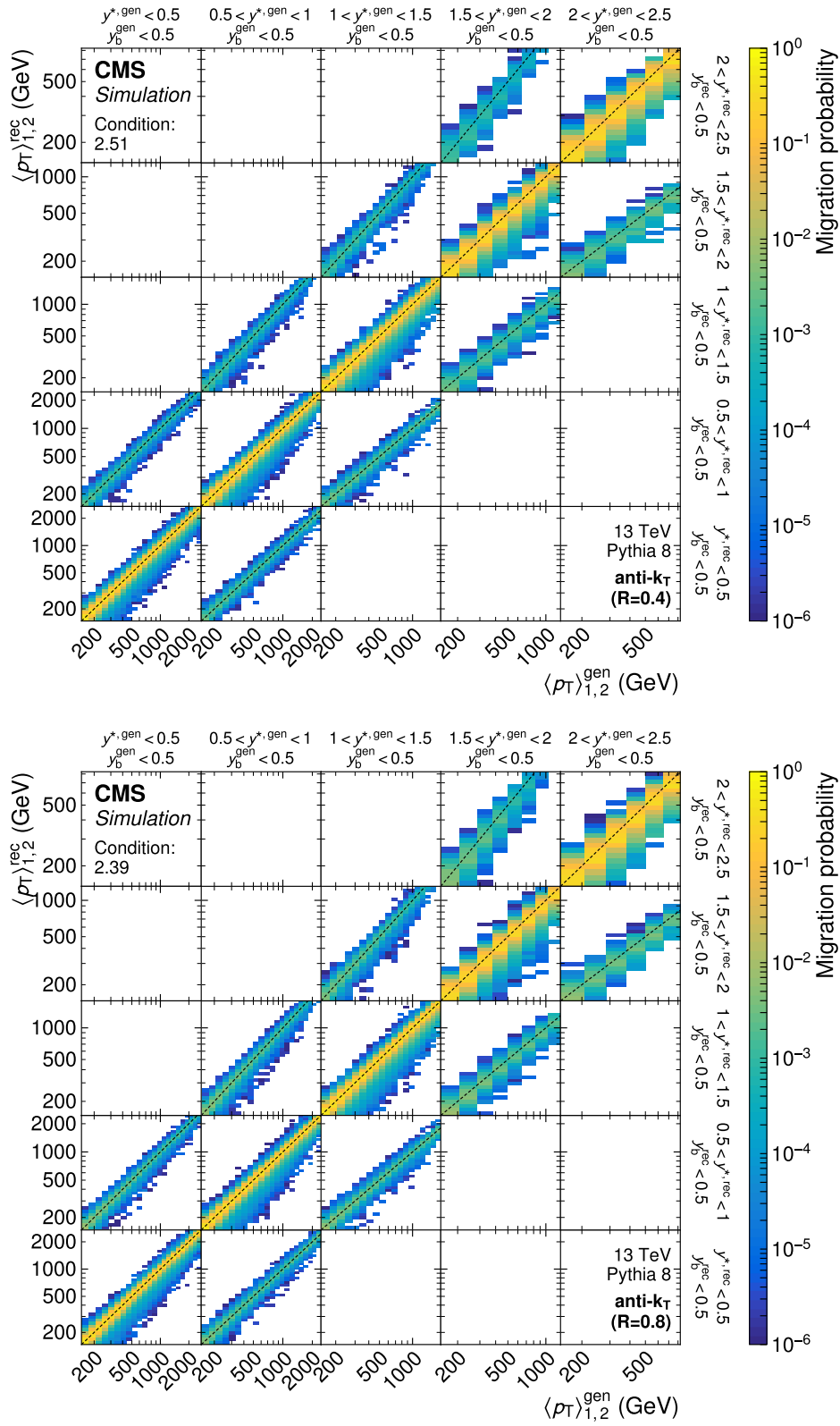


Figure 15: Partial response matrices for the 3D measurements as a function of $\langle p_T \rangle_{1,2}$ using jets with $R = 0.4$ (upper) and 0.8 (lower), shown here for the five rapidity regions with $y_b < 0.5$. The details correspond to those of Fig. 2.

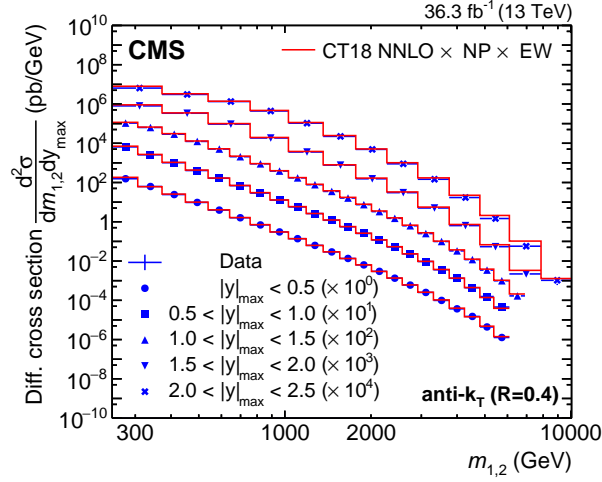


Figure 16: Overview of the 2D dijet cross section as a function of $m_{1,2}$ in all 5 $|y|_{\max}$ regions, using jets with $R = 0.4$. The details correspond to those of Fig. 8.

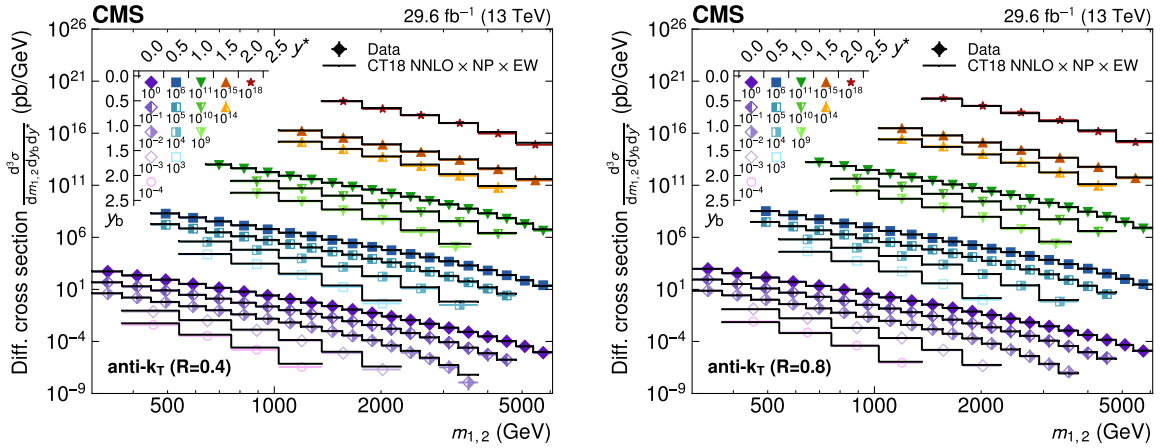


Figure 17: Overview of the 3D dijet cross section as a function of $m_{1,2}$ in all 15 (y^*, y_b) regions, using jets with $R = 0.4$ (left) and 0.8 (right). The details correspond to those of Fig. 8.

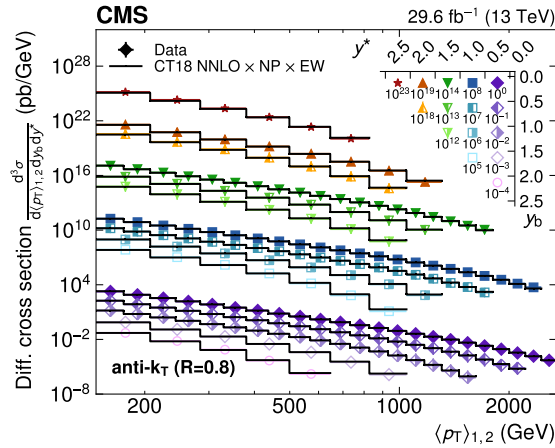


Figure 18: Overview of the 3D dijet cross section as a function of $\langle p_T \rangle_{1,2}$ in all 15 (y^*, y_b) regions, using jets with $R = 0.8$. The details correspond to those of Fig. 8.

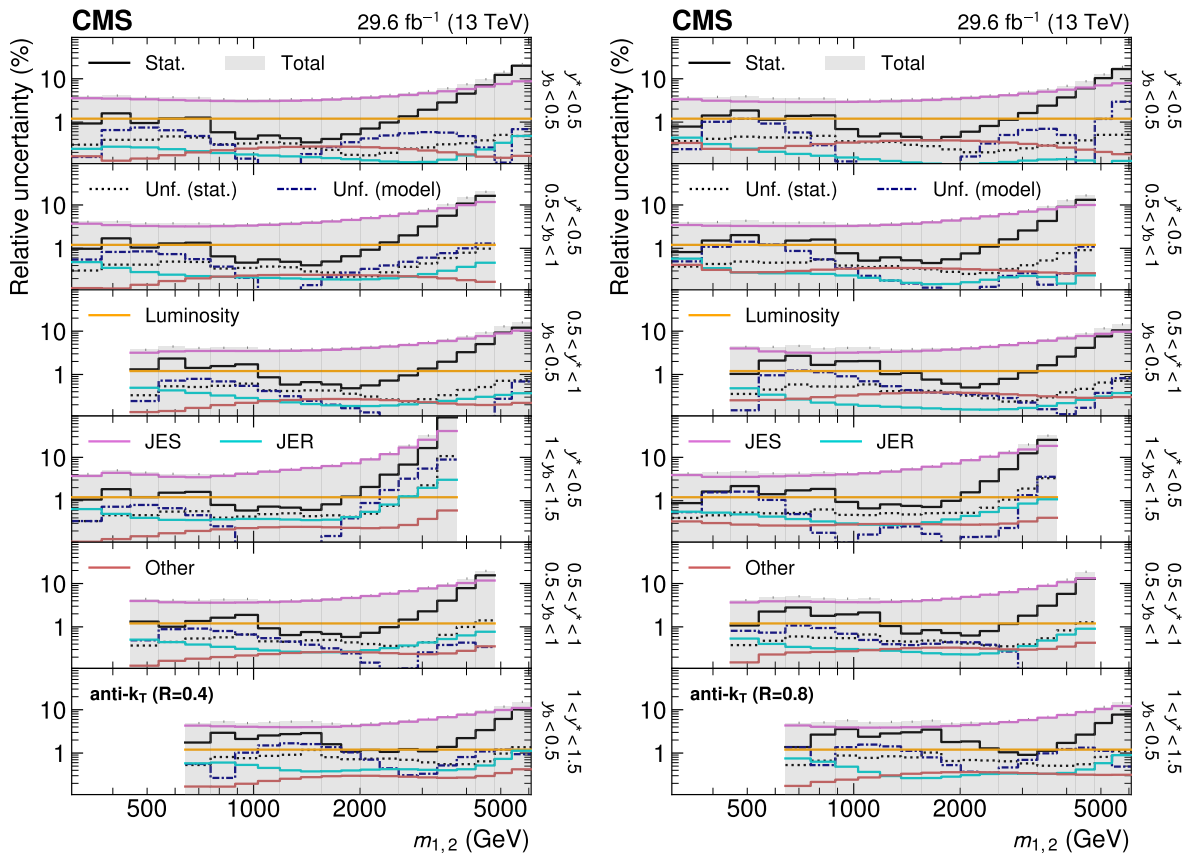


Figure 19: Breakdown of the experimental uncertainty for the 3D measurements as a function of $m_{1,2}$ using jets with $R = 0.4$ (left) and 0.8 (right), in six out of 15 (y^*, y_b) bins. The details correspond to those of Fig. 4.

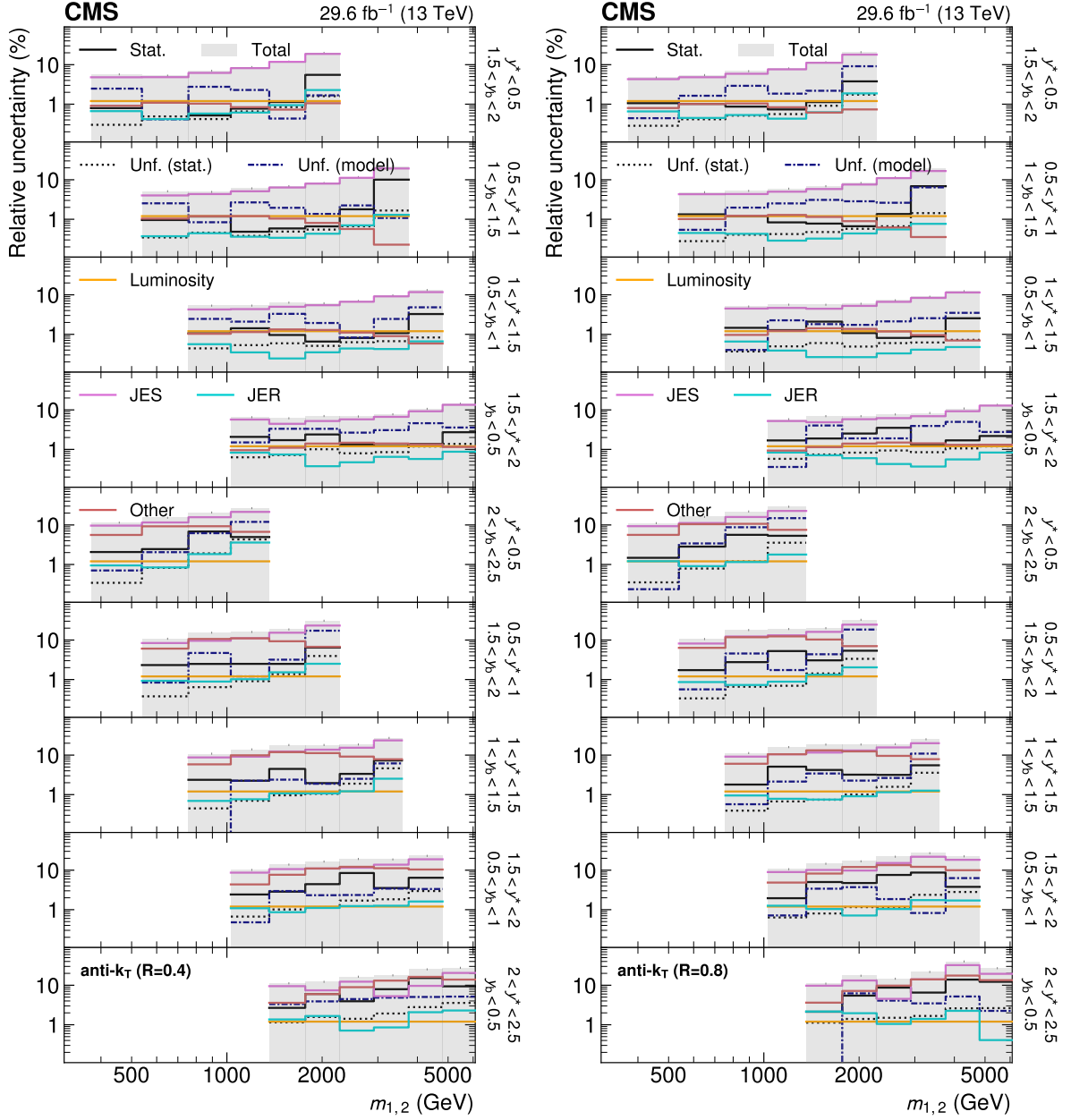


Figure 20: (continuation of Fig. 19) Breakdown of the experimental uncertainty for the 3D measurements as a function of $m_{1,2}$ using jets with $R = 0.4$ (left) and 0.8 (right), in the remaining nine out of 15 (y^* , y_b) bins. The details correspond to those of Fig. 4.

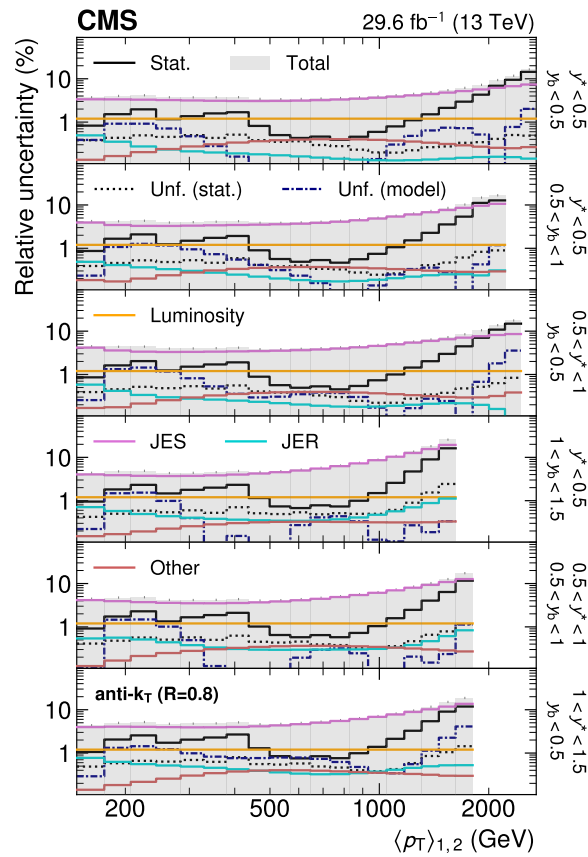


Figure 21: Breakdown of the experimental uncertainty for the 3D measurements as a function of $\langle p_T \rangle_{1,2}$ using jets with $R = 0.8$, in six out of 15 (y^*, y_b) bins. The details correspond to those of Fig. 4.

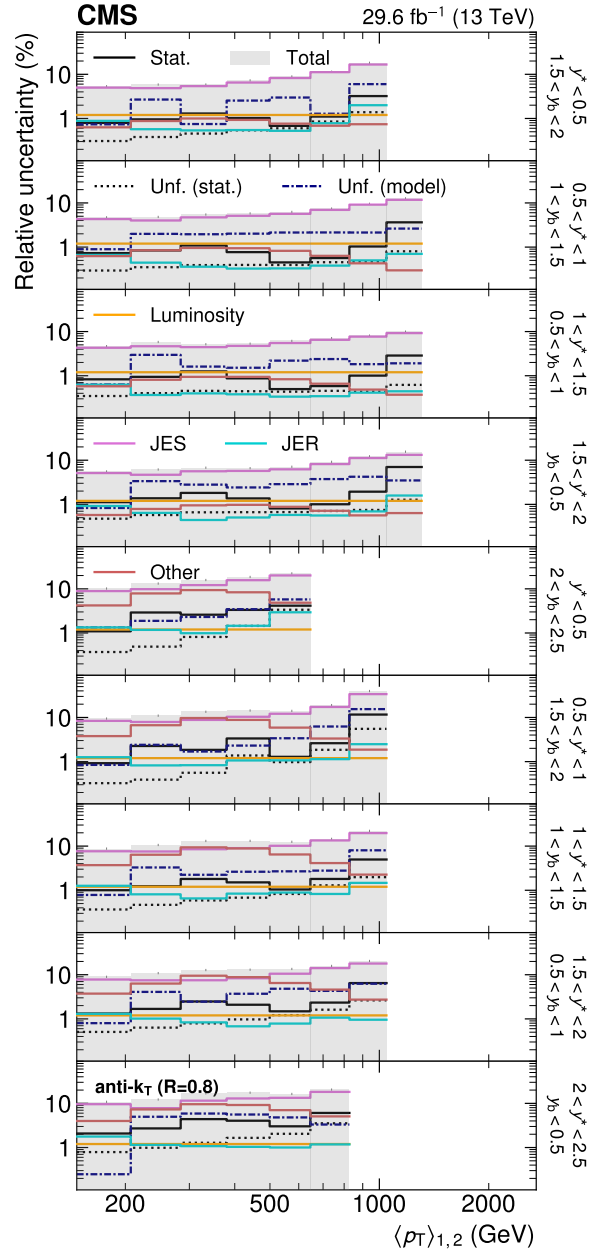


Figure 22: (continuation of Fig. 21) Breakdown of the experimental uncertainty for the 3D measurements as a function of $\langle p_T \rangle_{1,2}$ using jets with $R = 0.8$, in the remaining nine out of 15 (y^*, y_b) bins. The details correspond to those of Fig. 4.

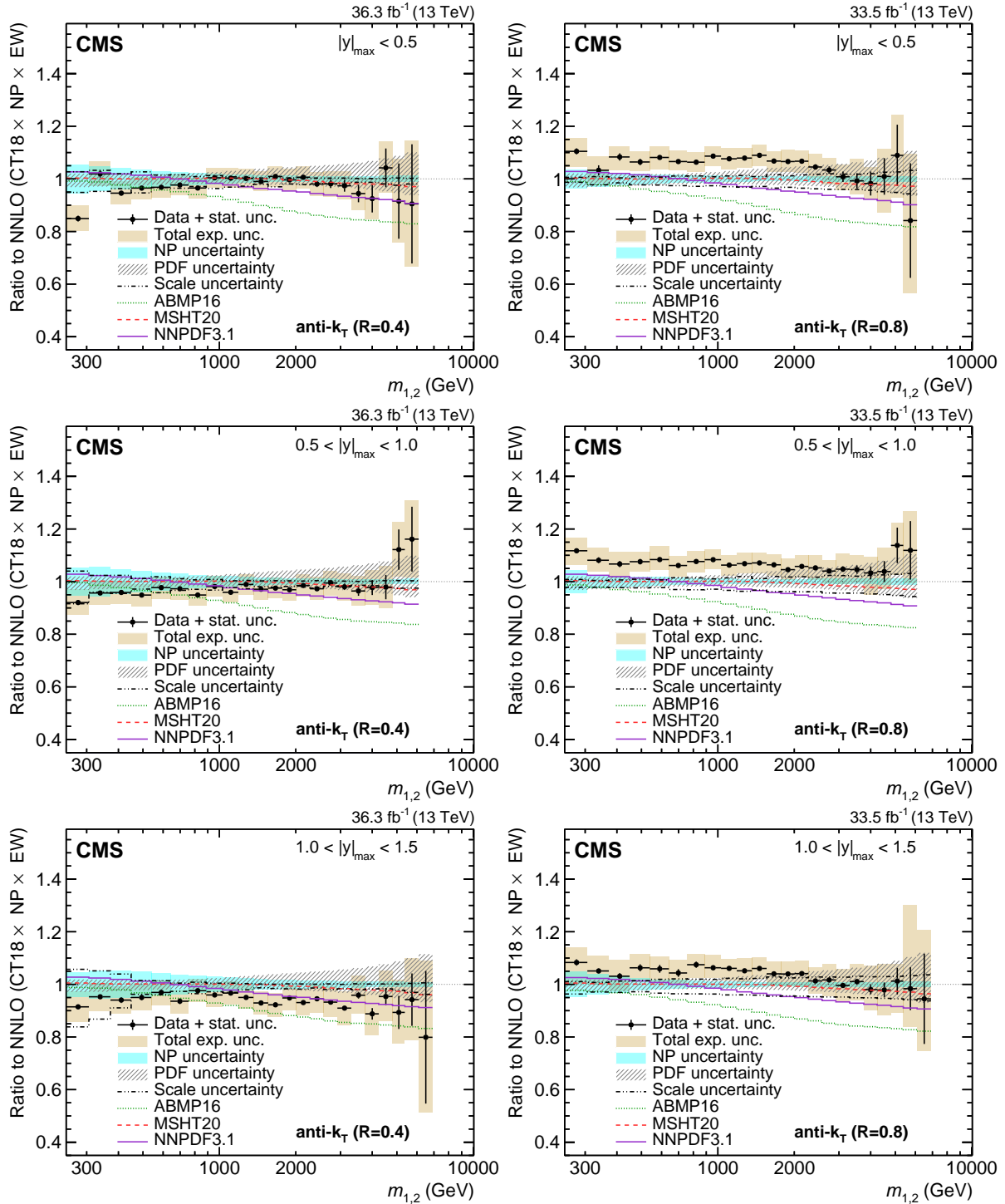


Figure 23: Comparison of the 2D dijet cross section for jets with $R = 0.4$ (left) and 0.8 (right) as a function of $m_{1,2}$ to fixed-order theoretical calculations at NNLO, shown here for three inner $|y|_{\max}$ regions. The details correspond to those of Fig. 9.

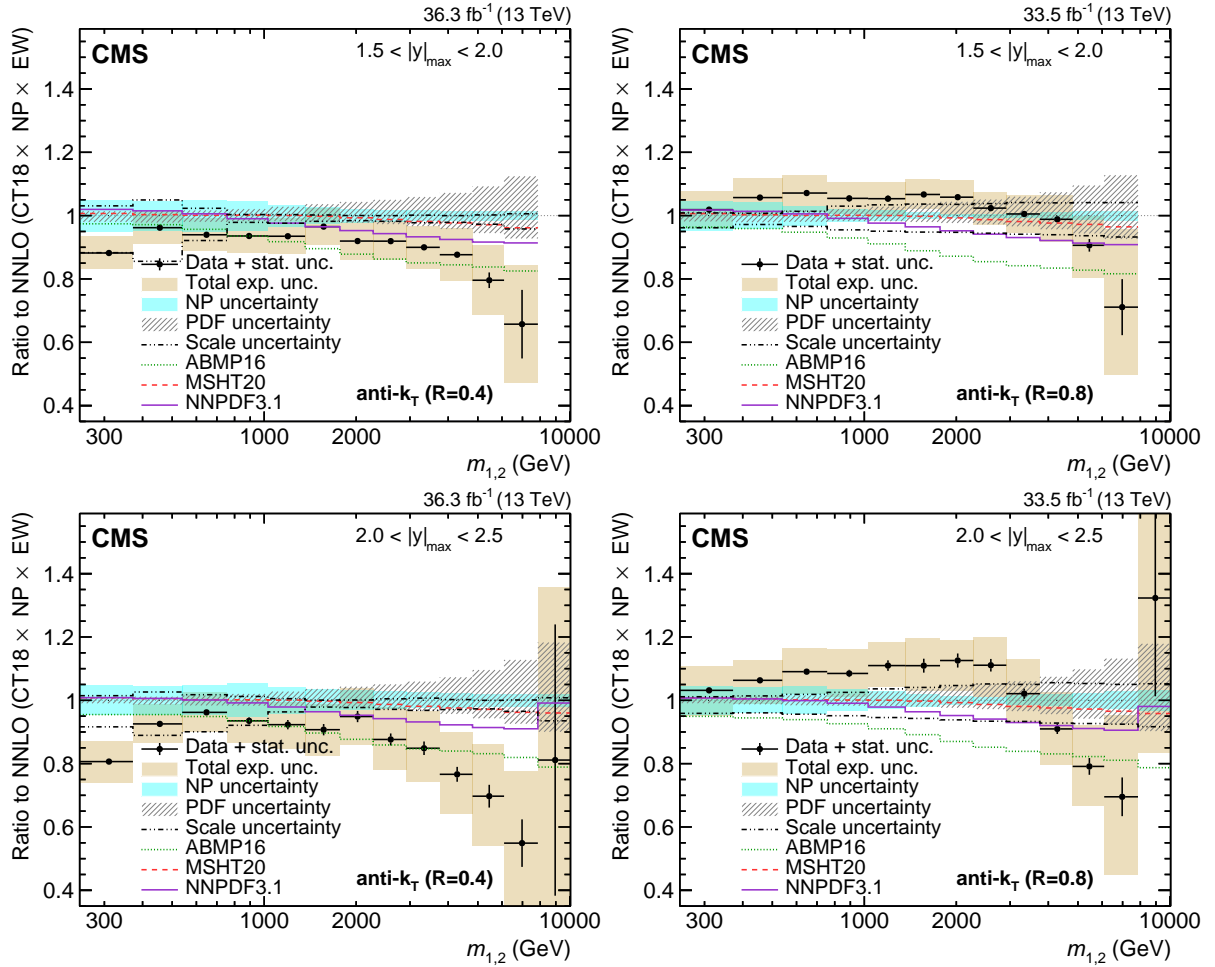


Figure 24: (continuation of Fig. 23) Comparison of the 2D dijet cross section for jets with $R = 0.4$ (left) and 0.8 (right) as a function of $m_{1,2}$ to fixed-order theoretical calculations at NNLO, shown here for two outermost $|y|_{\max}$ regions. The details correspond to those of Fig. 9.

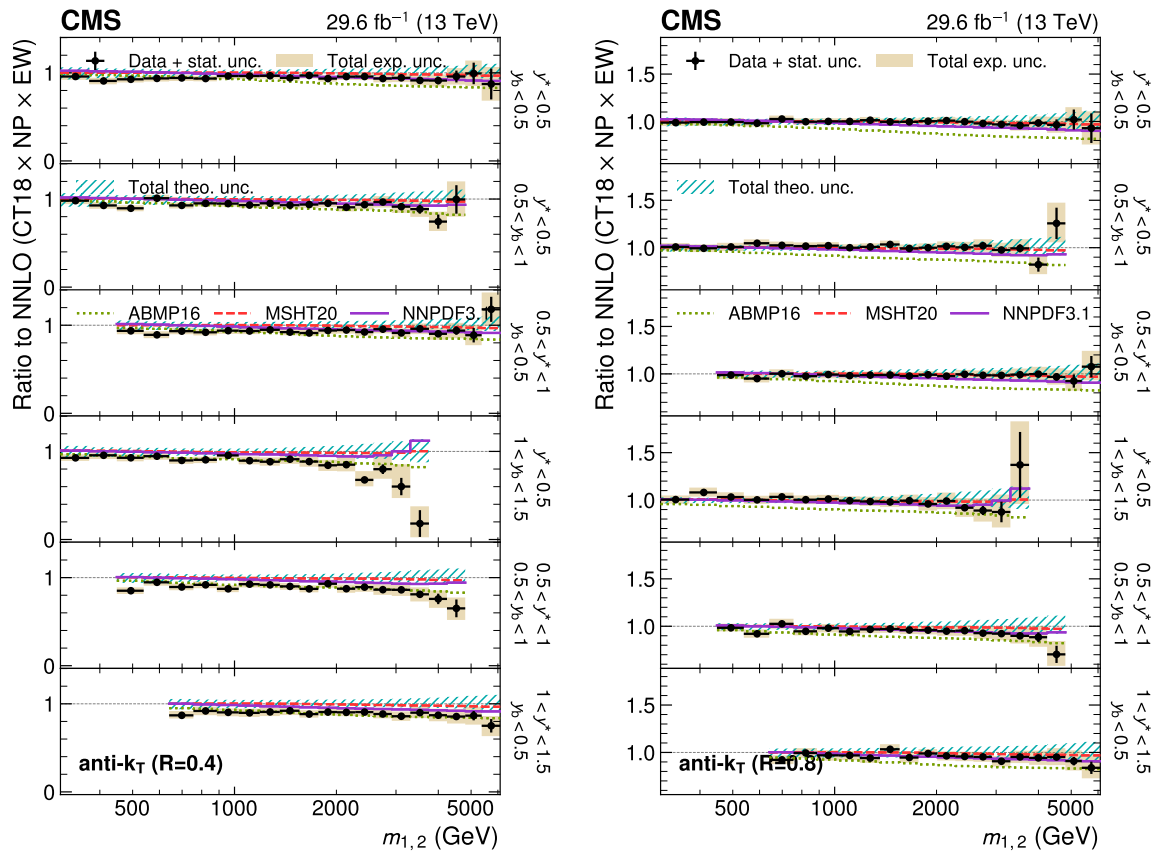


Figure 25: Comparison of the 3D dijet cross section as a function of $m_{1,2}$ to fixed-order theoretical calculations at NNLO, using jets with $R = 0.4$ (left) and 0.8 (right), in six out of the total 15 (y^*, y_b) bins. The details correspond to those of Fig. 10.

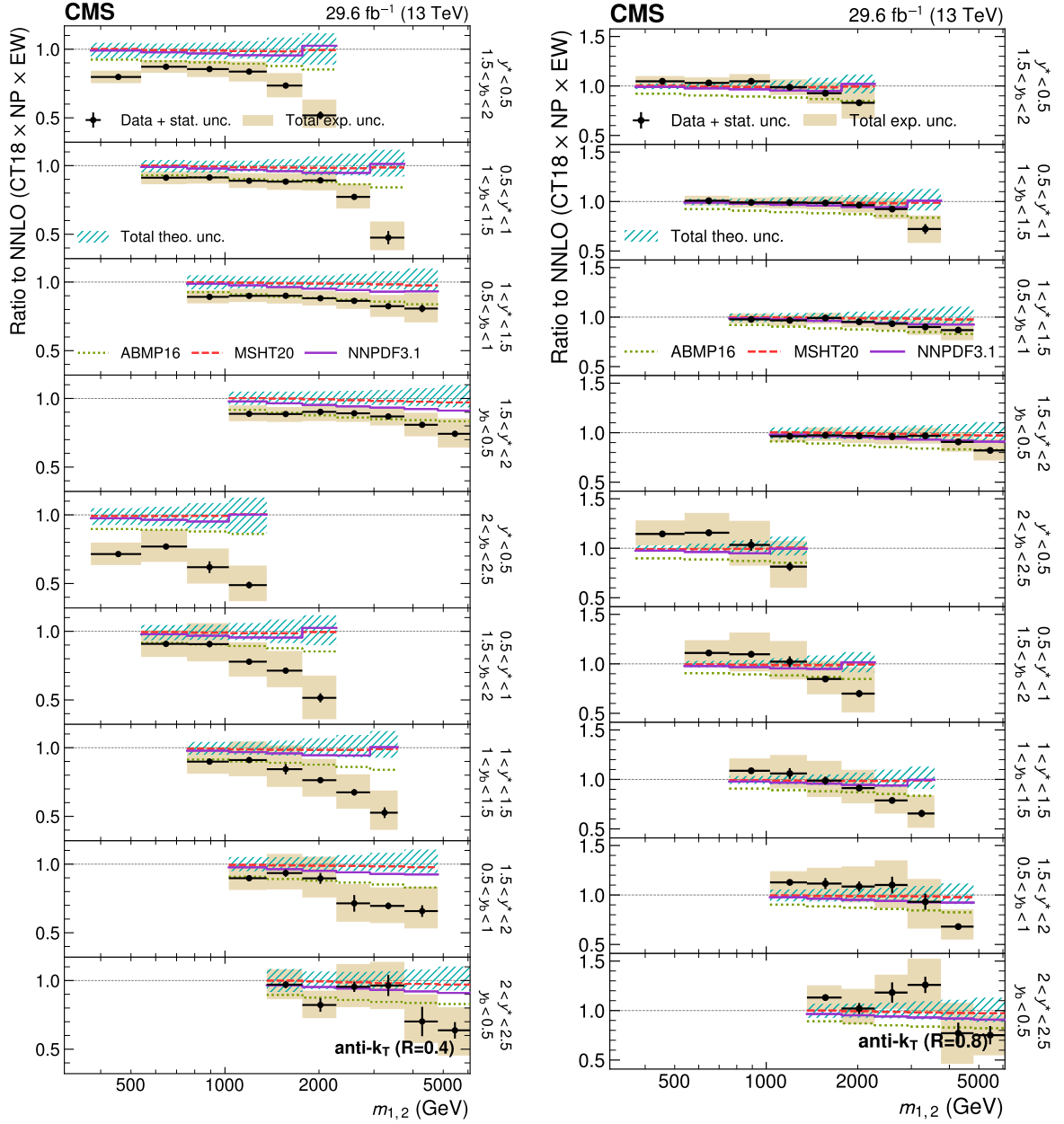


Figure 26: (continuation of Fig. 25) Comparison of the 3D dijet cross section as a function of $m_{1,2}$ to fixed-order theoretical calculations at NNLO, using jets with $R = 0.4$ (left) and 0.8 (right), in the remaining nine out of 15 (y^* , y_b) bins. The details correspond to those of Fig. 10.

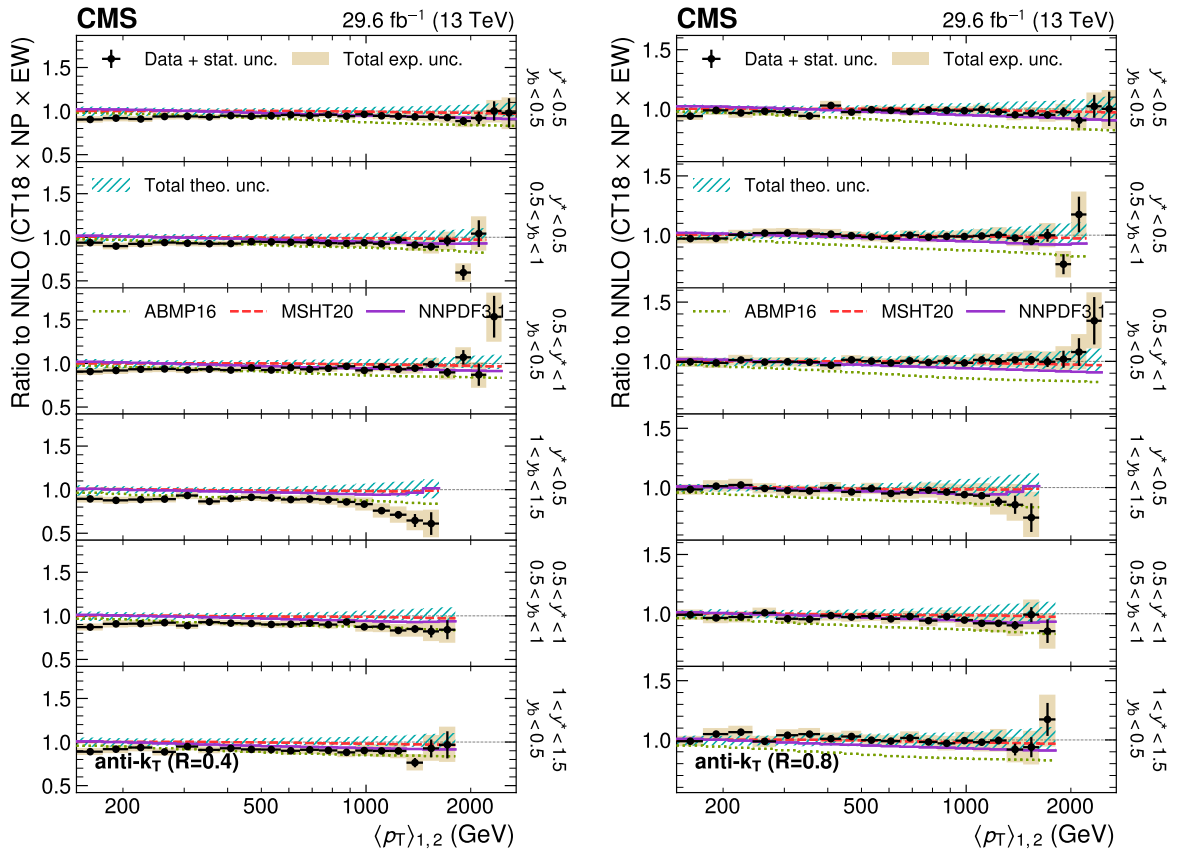


Figure 27: Comparison of the 3D dijet cross section as a function of $\langle p_T \rangle_{1,2}$ to fixed-order theoretical calculations at NNLO, using jets with $R = 0.4$ (left) and 0.8 (right), in six out of the total 15 (y^*, y_b) bins. The details correspond to those of Fig. 10.

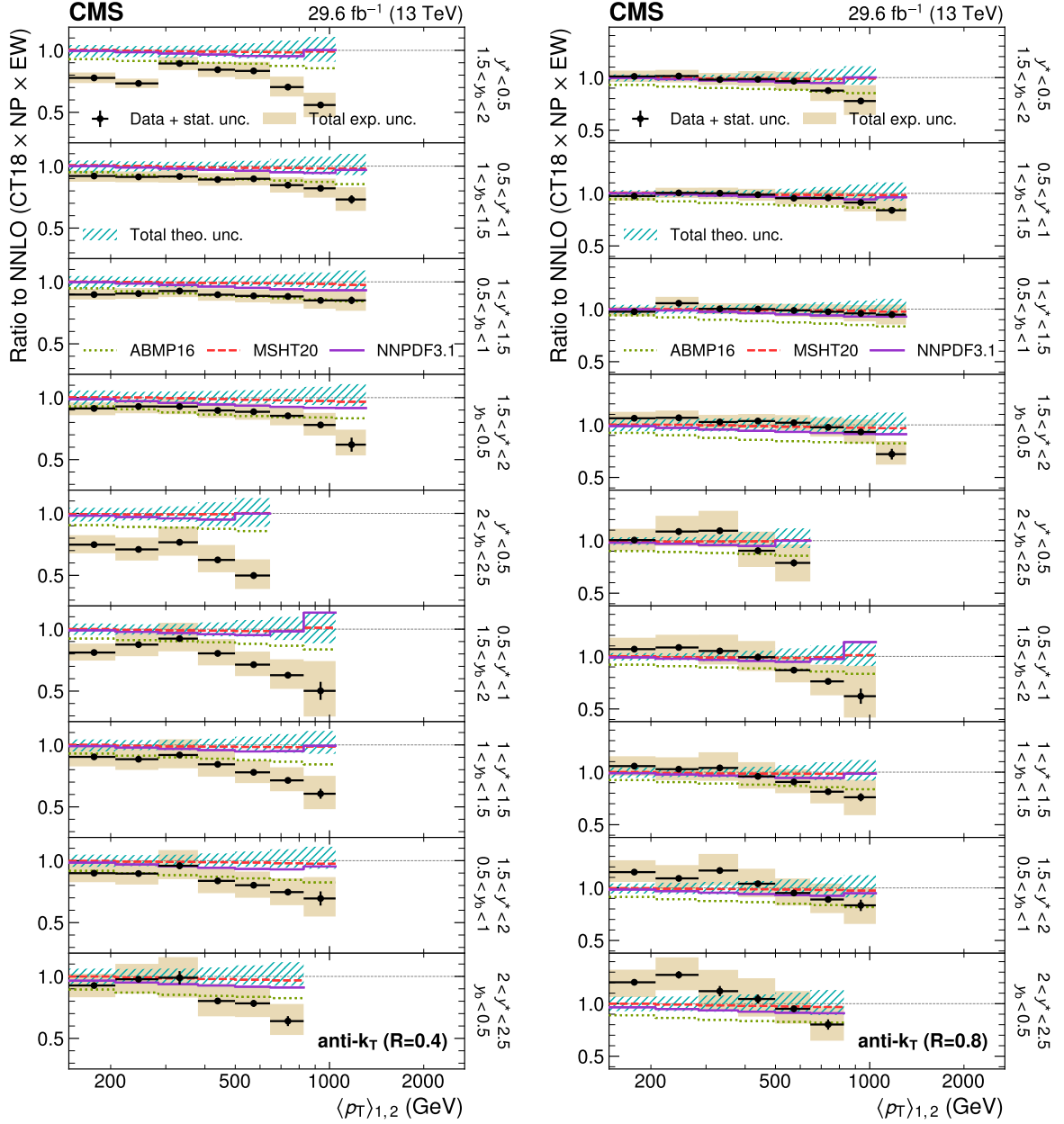








Figure 28: (continuation of Fig. 27) Comparison of the 3D dijet cross section as a function of $\langle p_T \rangle_{1,2}$ to fixed-order theoretical calculations at NNLO, using jets with $R = 0.4$ (left) and 0.8 (right), in the remaining nine out of 15 (y^*, y_b) bins. The details correspond to those of Fig. 10.

S. Keshri , S. Thakur 

Beihang University, Beijing, China

T. Cheng , Q. Guo, T. Javaid⁸ , M. Mittal , L. Yuan 






Department of Physics, Tsinghua University, Beijing, China

G. Bauer⁹, Z. Hu , K. Yi^{9,10} 

Institute of High Energy Physics, Beijing, China

G.M. Chen⁸ , H.S. Chen⁸ , M. Chen⁸ , F. Iemmi , C.H. Jiang, A. Kapoor , H. Liao , Z.-A. Liu¹¹ , F. Monti , R. Sharma , J.N. Song, J. Tao , C. Wang, J. Wang , H. Zhang 


State Key Laboratory of Nuclear Physics and Technology, Peking University, Beijing, China

A. Agapitos , Y. Ban , A. Levin , C. Li , Q. Li , X. Lyu, Y. Mao, S.J. Qian , X. Sun , D. Wang , H. Yang




Sun Yat-Sen University, Guangzhou, China

M. Lu , Z. You 

University of Science and Technology of China, Hefei, China

N. Lu 

Institute of Modern Physics and Key Laboratory of Nuclear Physics and Ion-beam Application (MOE) - Fudan University, Shanghai, China

X. Gao⁴ , D. Leggat, H. Okawa , Y. Zhang 

Zhejiang University, Hangzhou, Zhejiang, China

Z. Lin , C. Lu , M. Xiao 




Universidad de Los Andes, Bogota, Colombia

C. Avila , D.A. Barbosa Trujillo, A. Cabrera , C. Florez , J. Fraga , J.A. Reyes Vega

Universidad de Antioquia, Medellin, Colombia

J. Mejia Guisao , F. Ramirez , M. Rodriguez , J.D. Ruiz Alvarez 

University of Split, Faculty of Electrical Engineering, Mechanical Engineering and Naval Architecture, Split, Croatia

D. Giljanovic , N. Godinovic , D. Lelas , A. Sculac 









University of Split, Faculty of Science, Split, Croatia

M. Kovac , T. Sculac 




Institute Rudjer Boskovic, Zagreb, Croatia

P. Bargassa , V. Brigljevic , B.K. Chitroda , D. Ferencek , S. Mishra , A. Starodumov¹² , T. Susa 

University of Cyprus, Nicosia, Cyprus

A. Attikis , K. Christoforou , S. Konstantinou , J. Mousa , C. Nicolaou, F. Ptochos , P.A. Razis , H. Rykaczewski, H. Saka , A. Stepennov 

Charles University, Prague, Czech Republic

M. Finger , M. Finger Jr. , A. Kveton 

Escuela Politecnica Nacional, Quito, Ecuador

E. Ayala 




Universidad San Francisco de Quito, Quito, Ecuador

E. Carrera Jarrin 





Korea

G. Bak , P. Gwak , H. Kim , D.H. Moon 

Hanyang University, Seoul, Korea

E. Asilar , T.J. Kim , J. Park 

Korea University, Seoul, Korea

S. Choi , S. Han, B. Hong , K. Lee, K.S. Lee , J. Lim, J. Park, S.K. Park, J. Yoo 

Kyung Hee University, Department of Physics, Seoul, Korea

J. Goh 

Sejong University, Seoul, Korea

H. S. Kim , Y. Kim, S. Lee



Seoul National University, Seoul, Korea

J. Almond, J.H. Bhyun, J. Choi , S. Jeon , J. Kim , J.S. Kim, S. Ko , H. Kwon , H. Lee , S. Lee, B.H. Oh , S.B. Oh , H. Seo , U.K. Yang, I. Yoon 

University of Seoul, Seoul, Korea

W. Jang , D.Y. Kang, Y. Kang , D. Kim , S. Kim , B. Ko, J.S.H. Lee , Y. Lee , J.A. Merlin, I.C. Park , Y. Roh, I.J. Watson , S. Yang 

Yonsei University, Department of Physics, Seoul, Korea

S. Ha , H.D. Yoo 

Sungkyunkwan University, Suwon, Korea

M. Choi , M.R. Kim , H. Lee, Y. Lee , I. Yu 


College of Engineering and Technology, American University of the Middle East (AUM), Dasman, Kuwait

T. Beyrouthy, Y. Maghrbi 

Riga Technical University, Riga, Latvia

K. Dreimanis , A. Gaile , G. Pikurs, A. Potrebko , M. Seidel , V. Veckalns⁵⁵ 

University of Latvia (LU), Riga, Latvia

N.R. Strautnieks 


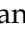




Vilnius University, Vilnius, Lithuania

M. Ambrozas , A. Juodagalvis , A. Rinkevicius , G. Tamulaitis 








National Centre for Particle Physics, Universiti Malaya, Kuala Lumpur, Malaysia

N. Bin Norjoharuddeen , I. Yusuff⁵⁶ , Z. Zolkapli

Universidad de Sonora (UNISON), Hermosillo, Mexico

J.F. Benitez , A. Castaneda Hernandez , H.A. Encinas Acosta, L.G. Gallegos Maríñez, M. León Coello , J.A. Murillo Quijada , A. Sehrawat , L. Valencia Palomo 

Centro de Investigacion y de Estudios Avanzados del IPN, Mexico City, Mexico

G. Ayala , H. Castilla-Valdez , E. De La Cruz-Burelo , I. Heredia-De La Cruz⁵⁷ , R. Lopez-Fernandez , C.A. Mondragon Herrera, D.A. Perez Navarro , A. Sánchez Hernández 

Universidad Iberoamericana, Mexico City, Mexico

C. Oropeza Barrera , M. Ramírez García 

Benemerita Universidad Autonoma de Puebla, Puebla, Mexico

I. Pedraza , H.A. Salazar Ibarguen , C. Uribe Estrada 

University of Montenegro, Podgorica, Montenegro

I. Bubanja, N. Raicevic 

University of Canterbury, Christchurch, New Zealand

P.H. Butler 

National Centre for Physics, Quaid-I-Azam University, Islamabad, Pakistan

A. Ahmad , M.I. Asghar, A. Awais , M.I.M. Awan, H.R. Hoorani , W.A. Khan 



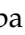


AGH University of Krakow, Faculty of Computer Science, Electronics and Telecommunications, Krakow, Poland

V. Avati, L. Grzanka , M. Malawski 

National Centre for Nuclear Research, Swierk, Poland

H. Bialkowska , M. Bluj , B. Boimska , M. Górski , M. Kazana , M. Szeleper , P. Zalewski 


Institute of Experimental Physics, Faculty of Physics, University of Warsaw, Warsaw, Poland

K. Bunkowski , K. Doroba , A. Kalinowski , M. Konecki , J. Krolikowski 



Warsaw University of Technology, Warsaw, Poland

K. Pozniak , W. Zabolotny 

Laboratório de Instrumentação e Física Experimental de Partículas, Lisboa, Portugal

M. Araujo , D. Bastos , C. Beirão Da Cruz E Silva , A. Boletti , M. Bozzo , P. Faccioli , M. Gallinaro , J. Hollar , N. Leonardo , T. Niknejad , M. Pisano , J. Seixas , J. Varela







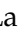
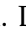

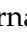


Faculty of Physics, University of Belgrade, Belgrade, Serbia

P. Adzic , P. Milenovic 

VINCA Institute of Nuclear Sciences, University of Belgrade, Belgrade, Serbia

M. Dordevic , J. Milosevic , V. Rekovic




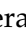


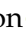
Centro de Investigaciones Energéticas Medioambientales y Tecnológicas (CIEMAT), Madrid, Spain

M. Aguilar-Benitez, J. Alcaraz Maestre , M. Barrio Luna, Cristina F. Bedoya , M. Cepeda , M. Cerrada , N. Colino , B. De La Cruz , A. Delgado Peris , D. Fernández Del Val , J.P. Fernández Ramos , J. Flix , M.C. Fouz , O. Gonzalez Lopez , S. Goy Lopez , J.M. Hernandez , M.I. Josa , J. León Holgado , D. Moran , Á. Navarro Tobar , C. Perez Dengra , A. Pérez-Calero Yzquierdo , J. Puerta Pelayo , I. Redondo , D.D. Redondo Ferrero , L. Romero, S. Sánchez Navas , L. Urda Gómez , J. Vazquez Escobar , C. Willmott





Universidad Autónoma de Madrid, Madrid, Spain

J.F. de Trocóniz 

Universidad de Oviedo, Instituto Universitario de Ciencias y Tecnologías Espaciales de Asturias (ICTEA), Oviedo, Spain

B. Alvarez Gonzalez , J. Cuevas , J. Fernandez Menendez , S. Folgueras , I. Gonzalez Caballero , J.R. González Fernández , E. Palencia Cortezon , C. Ramón Álvarez , V. Rodríguez Bouza , A. Soto Rodríguez , A. Trapote , C. Vico Villalba , P. Vischia

Instituto de Física de Cantabria (IFCA), CSIC-Universidad de Cantabria, Santander, Spain

S. Bhowmik , S. Blanco Fernández , J.A. Brochero Cifuentes , I.J. Cabrillo 

J.P. Cumalat [ID](#), W.T. Ford [ID](#), A. Hassani [ID](#), G. Karathanasis [ID](#), E. MacDonald, N. Manganello [ID](#), F. Marini [ID](#), A. Perloff [ID](#), C. Savard [ID](#), N. Schonbeck [ID](#), K. Stenson [ID](#), K.A. Ulmer [ID](#), S.R. Wagner [ID](#), N. Zipper [ID](#)

Cornell University, Ithaca, New York, USA

J. Alexander [ID](#), S. Bright-Thonney [ID](#), X. Chen [ID](#), D.J. Cranshaw [ID](#), J. Fan [ID](#), X. Fan [ID](#), D. Gadkari [ID](#), S. Hogan [ID](#), J. Monroy [ID](#), J.R. Patterson [ID](#), J. Reichert [ID](#), M. Reid [ID](#), A. Ryd [ID](#), J. Thom [ID](#), P. Wittich [ID](#), R. Zou [ID](#)

Fermi National Accelerator Laboratory, Batavia, Illinois, USA

M. Albrow [ID](#), M. Alyari [ID](#), O. Amram [ID](#), G. Apollinari [ID](#), A. Apresyan [ID](#), L.A.T. Bauerdick [ID](#), D. Berry [ID](#), J. Berryhill [ID](#), P.C. Bhat [ID](#), K. Burkett [ID](#), J.N. Butler [ID](#), A. Canepa [ID](#), G.B. Cerati [ID](#), H.W.K. Cheung [ID](#), F. Chlebana [ID](#), G. Cummings [ID](#), J. Dickinson [ID](#), I. Dutta [ID](#), V.D. Elvira [ID](#), Y. Feng [ID](#), J. Freeman [ID](#), A. Gandrakota [ID](#), Z. Gece [ID](#), L. Gray [ID](#), D. Green, S. Grünendahl [ID](#), D. Guerrero [ID](#), O. Gutsche [ID](#), R.M. Harris [ID](#), R. Heller [ID](#), T.C. Herwig [ID](#), J. Hirschauer [ID](#), L. Horyn [ID](#), B. Jayatilaka [ID](#), S. Jindariani [ID](#), M. Johnson [ID](#), U. Joshi [ID](#), T. Klijnsma [ID](#), B. Klima [ID](#), K.H.M. Kwok [ID](#), S. Lammel [ID](#), D. Lincoln [ID](#), R. Lipton [ID](#), T. Liu [ID](#), C. Madrid [ID](#), K. Maeshima [ID](#), C. Mantilla [ID](#), D. Mason [ID](#), P. McBride [ID](#), P. Merkel [ID](#), S. Mrenna [ID](#), S. Nahn [ID](#), J. Ngadiuba [ID](#), D. Noonan [ID](#), V. Papadimitriou [ID](#), N. Pastika [ID](#), K. Pedro [ID](#), C. Pena⁸⁵ [ID](#), F. Ravera [ID](#), A. Reinsvold Hall⁸⁶ [ID](#), L. Ristori [ID](#), E. Sexton-Kennedy [ID](#), N. Smith [ID](#), A. Soha [ID](#), L. Spiegel [ID](#), J. Strait [ID](#), L. Taylor [ID](#), S. Tkaczyk [ID](#), N.V. Tran [ID](#), L. Uplegger [ID](#), E.W. Vaandering [ID](#), I. Zoi [ID](#)

University of Florida, Gainesville, Florida, USA

P. Avery [ID](#), D. Bourilkov [ID](#), L. Cadamuro [ID](#), P. Chang [ID](#), V. Cherepanov [ID](#), R.D. Field, E. Koenig [ID](#), M. Kolosova [ID](#), J. Konigsberg [ID](#), A. Korytov [ID](#), K.H. Lo, K. Matchev [ID](#), N. Menendez [ID](#), G. Mitselmakher [ID](#), A. Muthirakalayil Madhu [ID](#), N. Rawal [ID](#), D. Rosenzweig [ID](#), S. Rosenzweig [ID](#), K. Shi [ID](#), J. Wang [ID](#)

Florida State University, Tallahassee, Florida, USA

T. Adams [ID](#), A. Al Kadhim [ID](#), A. Askew [ID](#), N. Bower [ID](#), R. Habibullah [ID](#), V. Hagopian [ID](#), R. Hashmi [ID](#), R.S. Kim [ID](#), S. Kim [ID](#), T. Kolberg [ID](#), G. Martinez, H. Prosper [ID](#), P.R. Prova, O. Viazlo [ID](#), M. Wulansatiti [ID](#), R. Yohay [ID](#), J. Zhang

Florida Institute of Technology, Melbourne, Florida, USA

B. Alsufyani, M.M. Baarmand [ID](#), S. Butalla [ID](#), T. Elkafrawy¹⁶ [ID](#), M. Hohlmann [ID](#), R. Kumar Verma [ID](#), M. Rahmani, F. Yumiceva [ID](#)

University of Illinois Chicago, Chicago, USA, Chicago, USA

M.R. Adams [ID](#), C. Bennett, R. Cavanaugh [ID](#), S. Dittmer [ID](#), O. Evdokimov [ID](#), C.E. Gerber [ID](#), D.J. Hofman [ID](#), J.h. Lee [ID](#), D. S. Lemos [ID](#), A.H. Merrit [ID](#), C. Mills [ID](#), S. Nanda [ID](#), G. Oh [ID](#), D. Pilipovic [ID](#), T. Roy [ID](#), S. Rudrabhatla [ID](#), M.B. Tonjes [ID](#), N. Varelas [ID](#), X. Wang [ID](#), Z. Ye [ID](#), J. Yoo [ID](#)

The University of Iowa, Iowa City, Iowa, USA

M. Alhusseini [ID](#), D. Blend, K. Dilsiz⁸⁷ [ID](#), L. Emediato [ID](#), G. Karaman [ID](#), O.K. Köseyan [ID](#), J.-P. Merlo, A. Mestvirishvili⁸⁸ [ID](#), J. Nachtman [ID](#), O. Neogi, H. Ogul⁸⁹ [ID](#), Y. Onel [ID](#), A. Penzo [ID](#), C. Snyder, E. Tiras⁹⁰ [ID](#)

Johns Hopkins University, Baltimore, Maryland, USA

B. Blumenfeld [ID](#), L. Corcodilos [ID](#), J. Davis [ID](#), A.V. Gritsan [ID](#), L. Kang [ID](#), S. Kyriacou [ID](#), P. Maksimovic [ID](#), M. Roguljic [ID](#), J. Roskes [ID](#), S. Sekhar [ID](#), M. Swartz [ID](#), T.Á. Vámi [ID](#)

The University of Kansas, Lawrence, Kansas, USA

-
- ¹⁵Also at British University in Egypt, Cairo, Egypt
- ¹⁶Now at Ain Shams University, Cairo, Egypt
- ¹⁷Also at Purdue University, West Lafayette, Indiana, USA
- ¹⁸Also at Université de Haute Alsace, Mulhouse, France
- ¹⁹Also at Department of Physics, Tsinghua University, Beijing, China
- ²⁰Also at The University of the State of Amazonas, Manaus, Brazil
- ²¹Also at Erzincan Binali Yildirim University, Erzincan, Turkey
- ²²Also at University of Hamburg, Hamburg, Germany
- ²³Also at RWTH Aachen University, III. Physikalisches Institut A, Aachen, Germany
- ²⁴Also at Isfahan University of Technology, Isfahan, Iran
- ²⁵Also at Bergische University Wuppertal (BUW), Wuppertal, Germany
- ²⁶Also at Brandenburg University of Technology, Cottbus, Germany
- ²⁷Also at Forschungszentrum Jülich, Juelich, Germany
- ²⁸Also at CERN, European Organization for Nuclear Research, Geneva, Switzerland
- ²⁹Also at Institute of Physics, University of Debrecen, Debrecen, Hungary
- ³⁰Also at Institute of Nuclear Research ATOMKI, Debrecen, Hungary
- ³¹Now at Universitatea Babeş-Bolyai - Facultatea de Fizica, Cluj-Napoca, Romania
- ³²Also at Physics Department, Faculty of Science, Assiut University, Assiut, Egypt
- ³³Also at HUN-REN Wigner Research Centre for Physics, Budapest, Hungary
- ³⁴Also at Faculty of Informatics, University of Debrecen, Debrecen, Hungary
- ³⁵Also at Punjab Agricultural University, Ludhiana, India
- ³⁶Also at UPES - University of Petroleum and Energy Studies, Dehradun, India
- ³⁷Also at University of Visva-Bharati, Santiniketan, India
- ³⁸Also at University of Hyderabad, Hyderabad, India
- ³⁹Also at Indian Institute of Science (IISc), Bangalore, India
- ⁴⁰Also at IIT Bhubaneswar, Bhubaneswar, India
- ⁴¹Also at Institute of Physics, Bhubaneswar, India
- ⁴²Also at Deutsches Elektronen-Synchrotron, Hamburg, Germany
- ⁴³Now at Department of Physics, Isfahan University of Technology, Isfahan, Iran
- ⁴⁴Also at Sharif University of Technology, Tehran, Iran
- ⁴⁵Also at Department of Physics, University of Science and Technology of Mazandaran, Behshahr, Iran
- ⁴⁶Also at Italian National Agency for New Technologies, Energy and Sustainable Economic Development, Bologna, Italy
- ⁴⁷Also at Centro Siciliano di Fisica Nucleare e di Struttura Della Materia, Catania, Italy
- ⁴⁸Also at Università degli Studi Guglielmo Marconi, Roma, Italy
- ⁴⁹Also at Scuola Superiore Meridionale, Università di Napoli 'Federico II', Napoli, Italy
- ⁵⁰Also at Fermi National Accelerator Laboratory, Batavia, Illinois, USA
- ⁵¹Also at Laboratori Nazionali di Legnaro dell'INFN, Legnaro, Italy
- ⁵²Also at Università di Napoli 'Federico II', Napoli, Italy
- ⁵³Also at Consiglio Nazionale delle Ricerche - Istituto Officina dei Materiali, Perugia, Italy
- ⁵⁴Also at IRFU, CEA, Université Paris-Saclay, Gif-sur-Yvette, France
- ⁵⁵Also at Riga Technical University, Riga, Latvia
- ⁵⁶Also at Department of Applied Physics, Faculty of Science and Technology, Universiti Kebangsaan Malaysia, Bangi, Malaysia
- ⁵⁷Also at Consejo Nacional de Ciencia y Tecnología, Mexico City, Mexico
- ⁵⁸Also at Trincomalee Campus, Eastern University, Sri Lanka, Nilaveli, Sri Lanka
- ⁵⁹Also at INFN Sezione di Pavia, Università di Pavia, Pavia, Italy
- ⁶⁰Also at National and Kapodistrian University of Athens, Athens, Greece

⁶¹Also at Ecole Polytechnique Fédérale Lausanne, Lausanne, Switzerland

⁶²Also at Universität Zürich, Zurich, Switzerland

⁶³Also at Stefan Meyer Institute for Subatomic Physics, Vienna, Austria

⁶⁴Also at Laboratoire d'Annecy-le-Vieux de Physique des Particules, IN2P3-CNRS, Annecy-le-Vieux, France

⁶⁵Also at Near East University, Research Center of Experimental Health Science, Mersin, Turkey

⁶⁶Also at Konya Technical University, Konya, Turkey

⁶⁷Also at Izmir Bakircay University, Izmir, Turkey

⁶⁸Also at Adiyaman University, Adiyaman, Turkey

⁶⁹Also at Necmettin Erbakan University, Konya, Turkey

⁷⁰Also at Bozok Universitetesi Rektörlüğü, Yozgat, Turkey

⁷¹Also at Marmara University, Istanbul, Turkey

⁷²Also at Milli Savunma University, Istanbul, Turkey

⁷³Also at Kafkas University, Kars, Turkey

⁷⁴Also at Hacettepe University, Ankara, Turkey

⁷⁵Also at Istanbul University - Cerrahpasa, Faculty of Engineering, Istanbul, Turkey

⁷⁶Also at Ozyegin University, Istanbul, Turkey

⁷⁷Also at Vrije Universiteit Brussel, Brussel, Belgium

⁷⁸Also at School of Physics and Astronomy, University of Southampton, Southampton, United Kingdom

⁷⁹Also at University of Bristol, Bristol, United Kingdom

⁸⁰Also at IPPP Durham University, Durham, United Kingdom

⁸¹Also at Monash University, Faculty of Science, Clayton, Australia

⁸²Also at Università di Torino, Torino, Italy

⁸³Also at Bethel University, St. Paul, Minnesota, USA

⁸⁴Also at Karamanoğlu Mehmetbey University, Karaman, Turkey

⁸⁵Also at California Institute of Technology, Pasadena, California, USA

⁸⁶Also at United States Naval Academy, Annapolis, Maryland, USA

⁸⁷Also at Bingol University, Bingol, Turkey

⁸⁸Also at Georgian Technical University, Tbilisi, Georgia

⁸⁹Also at Sinop University, Sinop, Turkey

⁹⁰Also at Erciyes University, Kayseri, Turkey

⁹¹Also at Horia Hulubei National Institute of Physics and Nuclear Engineering (IFIN-HH), Bucharest, Romania

⁹²Also at Texas A&M University at Qatar, Doha, Qatar

⁹³Also at Kyungpook National University, Daegu, Korea

⁹⁴Also at another institute or international laboratory covered by a cooperation agreement with CERN

⁹⁵Also at Universiteit Antwerpen, Antwerpen, Belgium

⁹⁶Also at Yerevan Physics Institute, Yerevan, Armenia

⁹⁷Also at Northeastern University, Boston, Massachusetts, USA

⁹⁸Now at another institute or international laboratory covered by a cooperation agreement with CERN

⁹⁹Also at Imperial College, London, United Kingdom

¹⁰⁰Also at Institute of Nuclear Physics of the Uzbekistan Academy of Sciences, Tashkent, Uzbekistan